LETTER

doi:10.1038/nature25742

Tissue stiffening coordinates morphogenesis by triggering collective cell migration *in vivo*

Elias H. Barriga[1,2], Kristian Franze[3], Guillaume Charras[1,2] & Roberto Mayor[1]

Collective cell migration is essential for morphogenesis, tissue remodelling and cancer invasion[1,2]. *In vivo*, groups of cells move in an orchestrated way through tissues. This movement involves mechanical as well as molecular interactions between cells and their environment. While the role of molecular signals in collective cell migration is comparatively well understood[1,2], how tissue mechanics influence collective cell migration *in vivo* remains unknown. Here we investigated the importance of mechanical cues in the collective migration of the *Xenopus laevis* neural crest cells, an embryonic cell population whose migratory behaviour has been likened to cancer invasion[3]. We found that, during morphogenesis, the head mesoderm underlying the cephalic neural crest stiffens. This stiffening initiates an epithelial-to-mesenchymal transition in neural crest cells and triggers their collective migration. To detect changes in their mechanical environment, neural crest cells use mechanosensation mediated by the integrin–vinculin–talin complex. By performing mechanical and molecular manipulations, we show that mesoderm stiffening is necessary and sufficient to trigger neural crest migration. Finally, we demonstrate that convergent extension of the mesoderm, which starts during gastrulation, leads to increased mesoderm stiffness by increasing the cell density underneath the neural crest. These results show that convergent extension of the mesoderm has a role as a mechanical coordinator of morphogenesis, and reveal a link between two apparently unconnected processes—gastrulation and neural crest migration—via changes in tissue mechanics. Overall, we demonstrate that changes in substrate stiffness can trigger collective cell migration by promoting epithelial-to-mesenchymal transition *in vivo*. More broadly, our results raise the idea that tissue mechanics combines with molecular effectors to coordinate morphogenesis[4].

The neural crest migrates as a mesenchymal cell population, and key transcription factors (for example, those in the Snail, Twist and Zeb families) are sufficient to promote epithelial-to-mesenchymal transition (EMT) *in vitro*[3,5]. During development, these factors are expressed well in advance of the onset of neural crest migration[3,6]; however it is unclear whether they are sufficient to trigger cell migration or whether additional extrinsic factors are also needed. To test whether the onset of neural crest migration is determined by extrinsic factors, we used heterochronic tissue grafts to expose non- and pre-migratory neural crest to embryonic environments at different developmental stages. Here we define non- and pre-migratory neural crest as those cells that are not migrating (stage 13) or are about to start migrating (stage 20), respectively[7] (Fig. 1a). When grafted into a host at a migratory stage, non-migratory neural crest migrated, whereas migration was impaired if pre-migratory neural crest was grafted into a non-migratory host (Fig. 1b–e; graft controls in Extended Data Fig. 1a–d). Furthermore, when cultured *ex vivo* and exposed to the neural crest chemoattractant Sdf-1 (also known as Cxcl12), which controls directional neural crest migration *in vivo*[8], non- and pre-migratory neural crests were identically motile (Fig. 1f; Supplementary Video 1), indicating that the cells are intrinsically capable of migrating irrespective of their embryonic stage. Together, these observations suggest that changes in environmental factors regulate the onset of neural crest migration.

One possible source of environmental changes is modification of the extracellular matrix (ECM). However, we did not observe changes in fibronectin, the principal component of *Xenopus* cranial neural crest ECM[9], between non- and pre- migratory stages (Extended Data Fig. 2a–d). As both EMT and cell migration have been shown to be influenced by the mechanical properties of the cellular environment *in vitro*[10,11], we next characterized the tissue stiffness of developing *Xenopus* embryos using iAFM, an *in vivo* atomic force microscopy (AFM) approach[12]. As the cephalic neural crest uses head mesoderm as a substrate for migration, we directly measured the apparent elastic modulus of the mesoderm by removing the superficial epidermis (Fig. 1g; AFM controls in Extended Data Fig. 2g–j). When compared at non- and pre-migratory embryonic stages, the stiffness of the mesoderm in front of the neural crest gradually and substantially increased over time (Fig. 1h). Removal of fibronectin had no effect on elastic modulus (Extended Data Fig. 2e, f), confirming that fibronectin does not contribute to mesodermal stiffness[13]. We found a strong correlation between mesodermal stiffening and the onset of neural crest migration ($R = 0.82$, $n = 16$ embryos), suggesting that tissue stiffening may trigger neural crest collective cell migration (CCM) *in vivo*.

To test whether these changes in *in vivo* substrate stiffness are sufficient to trigger neural crest CCM, we cultured neural crests on fibronectin-coated hydrogels with stiffness values similar to those found in non- and pre-migratory mesoderm (Extended Data Fig. 2k–m). Remarkably, pre-migratory neural crest migrated towards Sdf-1 when explanted onto stiff substrates but not when explanted onto soft substrates (Fig. 1i and Supplementary Video 2). High-resolution imaging revealed that clusters or individual neural crest cells explanted onto stiff substrates formed larger protrusions than those explanted onto soft substrates (Extended Data Fig. 3a–c and Supplementary Video 3). Neural crest clusters, but not single cells, displayed directional motion towards Sdf-1 on stiff substrates (Extended Data Fig. 3d). These observations suggest that substrate stiffness can be sensed at the single cell level; however, directed motion is an emergent property arising from cell–cell interactions.

Furthermore, neural crest cultured on stiff, but not soft, substrates tended to disperse (Extended Data Fig. 3e–h and Supplementary Video 4), a characteristic of EMT[14]. Consequently, we found that a stiff substrate reduced the levels of the epithelial marker E-cadherin[2,14], whereas the expression of the mesenchymal marker N-cadherin[2,8,14] was increased (Extended Data Fig. 3i, j). Hence, environmental stiffening of the mesoderm may prime neural crest CCM by triggering EMT.

To confirm that the observed increase in mesodermal stiffness is important for neural crest migration *in vivo*, we next perturbed mesoderm stiffness using mechanical and molecular manipulations. Most developmental systems are under tension[15,16], which can

[1]Department of Cell and Developmental Biology, University College London, Gower Street, London WC1E 6BT, UK. [2]London Centre for Nanotechnology, University College London, Gower Street, London WC1H 0AH, UK. [3]Department of Physiology, Development and Neuroscience, University of Cambridge, Downing Street, Cambridge CB2 3DY, UK.

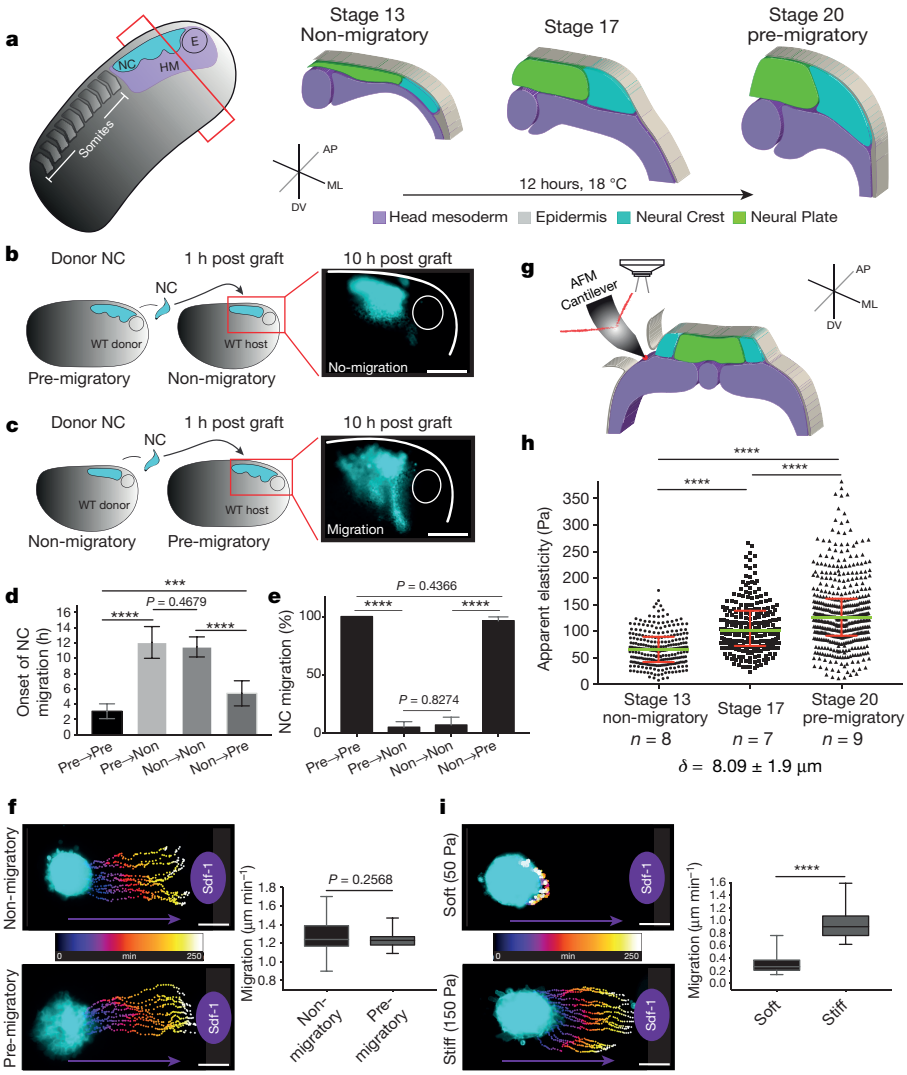

Figure 1 | Changes in environmental stiffness are required for neural crest CCM. a, Schematic cross-sections of neural crest development (AP, anteroposterior; ML, mediolateral; DV dorsoventral; NC, neural crest; HM, head mesoderm; E, eye). Cephalic neural crest originates from ectoderm at the border of the neural plate and undergoes EMT before migrating by using head mesoderm as substrate. **b**–**e**, Heterochronic grafts. **b**, Labelled pre-migratory neural crest (cyan) grafted into non-migratory hosts, a representative example of 'not-migrating' neural crest at 10 h post-graft is shown. WT, wild-type. **c**, Non-migratory neural crest (cyan) grafted into pre-migratory hosts, a representative example of 'migrating' neural crest at 10 h post-graft is shown. Scale bars, 150 μm (**b**, **c**). **d**, Onset of neural crest migration; *x*-axis labels indicate migratory status of donor→host. **e**, Percentage of migrating neural crests at 10 h post-graft. Histograms show mean, error bars represent s.d. (**d**) or s.e.m. (**e**); one-way analysis of variance (ANOVA), $P < 0.0001$; two-tailed *t*-test, $^{***}P < 0.0002$, $^{****}P < 0.0001$, CI = 95%, $n = 43$ embryos in **b**–**e**). **f**, **i**, Time colour-coded trajectories and quantification of speed of neural crest migration towards Sdf-1. **f**, Non-migratory versus pre-migratory neural crest. **i**, Pre-migratory neural crest plated on soft or stiff substrates. Box plots in **f** and **i** show the median, box edges represent the 25th and 75th percentiles, and whiskers show spread of data (two-tailed *t*-test, $^{****}P < 0.0001$; $n = 78$ cells (**f**); $n = 79$ cells (**i**)). **g**–**h**, *In vivo* atomic force microscopy (iAFM) measurements. **g**, iAFM measurement direct on mesoderm. **i**, Spread of data for each stage, green lines show median, red whiskers represent interquartile range (two-tailed Mann–Whitney *U*-test, $^{****}P < 0.0001$, CI = 95%; $n = 259$ (stage 13), $n = 236$ (stage 17) and $n = 461$ (stage 20) AFM indentations; n = number of embryos; δ = mean indentation depth). Scale bars, 100 μm (**f**, **i**). **b**, **c**, **f** and **i** show representative examples from three independent experiments; CI = 95%.

lead to strain-stiffening of the tissue, increasing its apparent elastic modulus[12,17–19]. To reduce the stiffness experienced by neural crest cells, we mechanically ablated the surrounding tissue, leading to a release of tension and hence to a decrease in strain stiffening. Tissue ablation in the anterior region of the embryo (Fig. 2a) led to reduced mesodermal stiffness compared to the non-ablated side, as recorded by iAFM (Fig. 2b), and inhibited neural crest migration (Fig. 2c, d; ablation controls in Extended Data Fig. 4a, b).

Next, we carried out molecular manipulation of mesoderm stiffness by targeted injections of inhibitors of myosin activity, which decreased tissue stiffness (Fig. 2e, f and Extended Data Fig. 4c, d). The injection of either a translation-blocking morpholino against myosin light chain 9 (*myl9*-MO) or a constitutively active form of myosin phosphatase (Mypt1(T696A), referred here as CA-MYPT) markedly decreased mesoderm stiffness and blocked neural crest migration, as shown by *in situ* hybridization of the migratory neural crest marker *snail2* (also known as *snai2*) (Fig. 2f–i). Similar inhibition of neural crest migration was observed in embryos in which wild-type neural crests were grafted into embryos injected with *myl9*-MO or CA-MYPT (Extended Data Fig. 5a–d; fibronectin deposition control in Extended Data Fig. 6a–g), ruling out an effect of the manipulation of myosin on the migratory capacities of the neural crest cells. These data show that a critical stiffness in the mesoderm is required to promote neural crest migration *in vivo*.

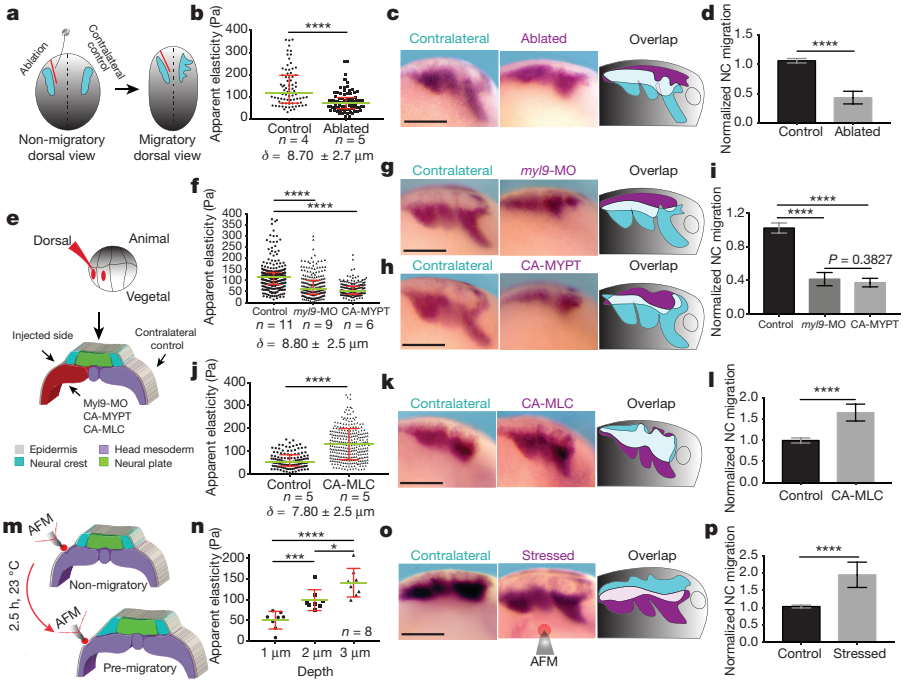

Figure 2 | Mesodermal stiffening is essential for neural crest CCM *in vivo*. **a**–**d**, Ablation experiments. **a**, Schematic showing ablation at non-migratory stages, and neural crest migration at stage 23 (migratory). **b**, iAFM measurements. $n = 78$ (control) and $n = 86$ (ablated) AFM indentations. **c**, Lateral views of embryos hybridized with a probe against *snail2* to analyse neural crest migration. **d**, Normalized neural crest migration ($n = 10$ embryos). **e**–**l**, Mesoderm-targeted injections. **e**, Embryos were injected into two dorso-vegetal blastomeres (prospective mesoderm). **f**, **j**, iAFM measurements. In **f**, $n = 294$ (control), $n = 224$ (*myl9*-MO), $n = 223$ (CA-MYPT); in **j**, $n = 120$ (control), $n = 301$ (CA-MLC). **g**, **h**, **k**, *snail2*-hybridized embryos. **i**, **l**, Normalized neural crest migration. $n = 25$ embryos (**i**); $n = 12$ embryos (**l**). **m**–**p**, Compression experiments. **m**, Schematic of AFM compression. **n**, Apparent elasticity plotted as a function of indentation depth ($n = 8$ embryos), green lines show median and whiskers represent the spread of data (excluding outliers). **o**, *snail2*-hybridized embryos. **p**, Normalized neural crest migration ($n = 13$ embryos). Overlap drawings in **c**, **g**, **h**, **k** and **o** are shown to facilitate comparison of neural crest migration, control neural crest (cyan) and treated neural crest (magenta). **b**, **f**, **j**, Direct iAFM measurements on mesoderm; green lines show median, red whiskers represent interquartile range; two-tailed Mann–Whitney *U* test, $****P < 0.0001$, CI = 95%, n = number of embryos, δ = mean maximum indentation depth. Histograms in **d**, **i**, **l** and **p** show mean, error bars represent s.d.; one-way ANOVA, $P < 0.0001$; two-tailed *t*-test, $*P = 0.014$, $***P < 0.001$, $****P < 0.0001$, CI = 95%). **c**, **g**, **h**, **k** and **o** show representative examples from three independent experiments. Scale bars, 200 μm.

We next investigated whether reaching this threshold stiffness in non-migratory embryos was sufficient to trigger premature neural crest migration. Injection of a constitutively active form of myosin light chain (DD-MLC, referred here as CA-MLC) into the mesoderm led to an early increase in tissue stiffness equivalent to that reached in pre-migratory embryos, and promoted premature neural crest migration (Fig. 2j–l; Extended Data Fig. 5e–g). To increase tissue stiffness without genetic or pharmacological manipulations, we applied locally a sustained compressive force on the embryos using iAFM (Fig. 2m; compression controls in Extended Data Fig. 4e–i), leading to strain stiffening[12,18,19] and premature neural crest migration (Fig. 2n–p). These results demonstrate that mesodermal stiffening is necessary and sufficient to trigger neural crest CCM *in vivo*.

To investigate how neural crest cells sense this increase in mesodermal stiffness, we perturbed signalling by inhibiting the integrin–vinculin–talin complex, which mediates mechanosensing in other systems[20]. We inhibited the integrin pathway in the neural crest by using a morpholino against *itgb1* (*itgb1*-MO) and dominant-negative forms of vinculin and talin. Inhibition of any of these mechanosensors led to a strong impairment of the onset of neural crest migration *in vivo* (Extended Data Fig. 7a–c), without significantly affecting attachment *in vitro*. These results show that the neural crest requires integrin–vinculin–talin for its migration, suggesting that this pathway is involved in mechanosensing by neural crest cells.

Our next goal was to examine the mechanisms underlying mesodermal stiffening *in vivo*. Modifications in ECM (for example, an increase in collagen fibres) have been proposed to affect tissue stiffness[21,22]; however, collagen is not expressed in the tissue during neural crest migration[23]. Together with our data that rules out fibronectin as a source of stiffening (Extended Data Fig. 2a–f), this suggests that changes in ECM are unlikely to be the cause of mesoderm stiffening in this system.

Although it has been proposed that myosin contractility increases tension locally, and thus stiffness of the dorsal mesoderm[13], our control experiments (Extended Data Figs 8a–e; 9a–h) suggest that actomyosin contractility is not essential for controlling head mesodermal stiffness during the stages at which the neural crest migrates. However, when we inhibited myosin in non-migratory embryos, mesoderm stiffness was reduced and neural crest migration was impaired (Fig. 2f–i and Extended Data Fig. 9a–c). This temporal difference in action is likely to be because myosin activity is required for the migration of mesoderm cells between non- and pre-migratory stages[13,24], which in turn indirectly affects subsequent mesoderm stiffness.

Another factor that controls tissue stiffness is cell density[12,25,26]. During development, mesoderm cells accumulate and intercalate in dorsal regions via convergent extension[24]. To test whether mesodermal cells accumulate underneath the neural crest, we measured mesodermal cell densities from non-migratory to pre-migratory stages. Cell densities increased towards the onset of neural crest migration (Fig. 3a–c), and furthermore, cell density directly correlated with mesoderm stiffening in all the treatments that affected migration ($R = 0.86$, $n = 16$ embryos) (Fig. 3d). These observations confirm that once cells have accumulated by convergent extension, the main contributor to mesoderm stiffness is cell density.

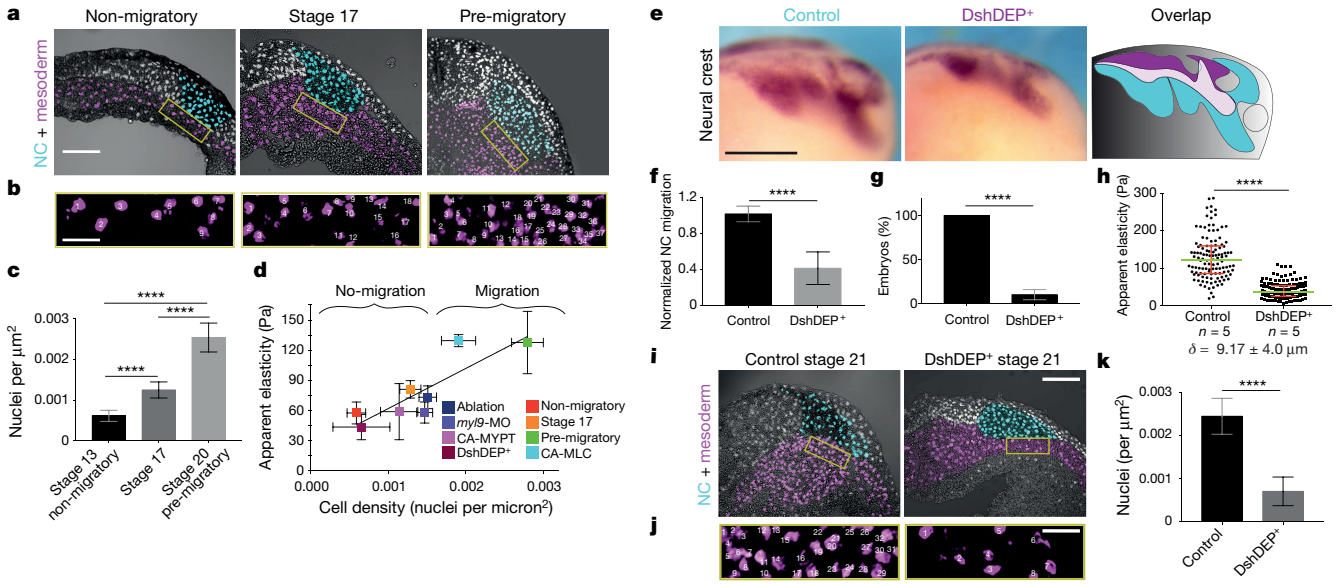

Figure 3 | PCP-dependent convergent extension is the driving force for mesodermal stiffening. a–d, Cell density analysis. **a**, Cross-sections of embryos at the indicated stages showing embryo morphology and nuclei pseudo-stained for neural crest (cyan) and mesoderm (magenta). **b**, Magnification of the areas outlined in **a**, used to quantify cell density. **c**, Nucleus density under the neural crest ($n = 27$ sections). **d**, Apparent elasticity of the head mesoderm as a function of cell density (Pearson test, $R = 0.8627$, $n = 16$ embryos). **e–k**, Effect of DshDEP$^+$. **e**, Lateral views and overlaps of control (cyan) or DshDEP$^+$ (magenta) *snail2*-hybridized embryos. **f**, Normalized neural crest migration ($n = 14$ embryos). **g**, Percentage of embryos displaying neural crest migration. **h**, Direct iAFM measurement on mesoderm. Green lines show median, red whiskers represent interquartile range (two-tailed Mann–Whitney *U*-test, $^{****}P < 0.0001$, CI = 95%; $n = 120$ (control), $n = 148$ embryos (DshDEP$^+$), δ = mean maximum indentation depth). **i**, Overlay showing embryo morphology and nuclei. **j**, Magnification of areas outlined in **i**, used to quantify cell density. **k**, Nucleus density under the neural crest, ($n = 11$ embryos). Histograms in **c**, **f**, **g** and **k** show mean; error bars, s.d. (**c**, **f**, **k**) or s.e.m. (**g**). One-way ANOVA, $P < 0.0001$; two-tailed *t*-test, $^{****}P < 0.0001$, CI = 95%. Scale bars: 100 µm (**a, i**), 50 µm (**b, j**) 200 µm (**e**). **a**, **b**, **e**, **i** and **j** show representative examples from three independent experiments.

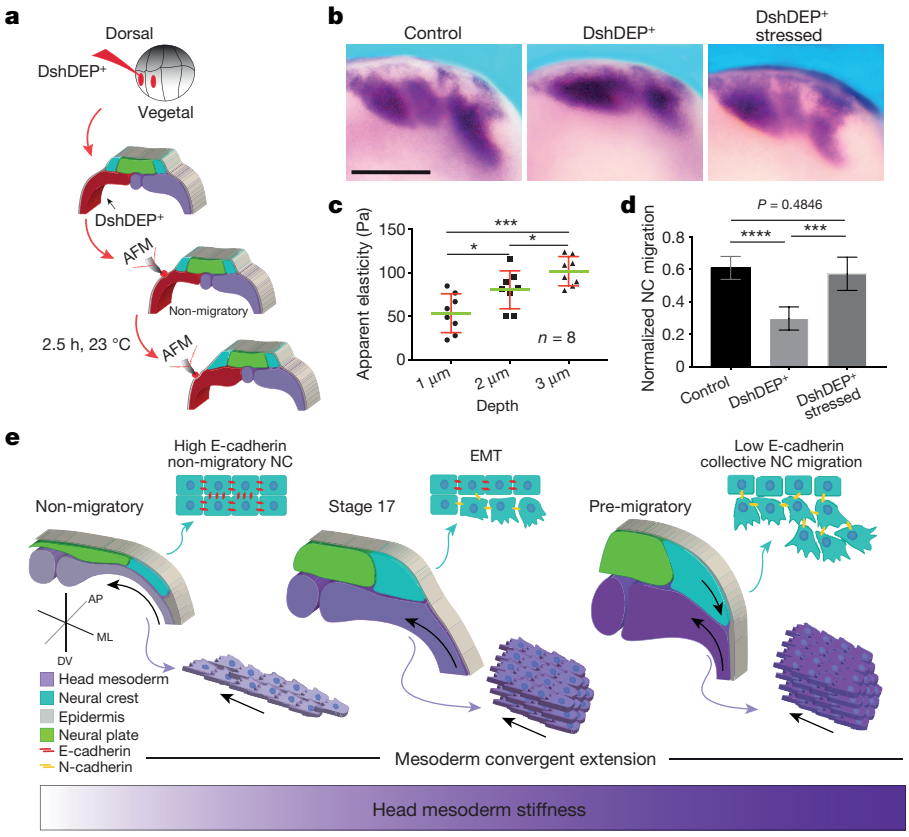

Figure 4 | PCP loss-of-function is mechanically rescued by extrinsically inducing mesodermal stiffening. a–d, Mechanical rescue of DshDEP$^+$-induced defects. **a**, Graphical description of compression experiments. **b**, Lateral view of *snail2*-hybridized embryos. Scale bar, 200 µm. **c**, Induced apparent elasticity plotted as a function of indentation depth. $n = 8$ embryos; green lines represent median and whiskers show the spread of data (excluding outliers). **d**, Normalized neural crest migration. $n = 19$ embryos. **b** shows representative examples from three independent experiments. Histograms in **d** show mean and error bars show s.d. In **c** and **d**, one-way ANOVA, $P < 0.0003$; two-tailed *t*–test, $^{*}P < 0.045$, $^{***}P < 0.0002$, $^{****}P < 0.0001$, CI = 95%. **e**, Schematic representing how mechanical interaction between mesoderm and neural crest coordinates morphogenesis. As convergent extension progresses, the mesoderm stiffens, and in turn, neural crest EMT is triggered and CCM proceeds.

To validate the role of convergent extension in mesoderm stiffening, we specifically inhibited the planar cell polarity pathway (PCP) in the mesoderm with targeted injections of the PCP inhibitor DshDEP$^+$ (ref. 24). Inhibition of PCP signalling impaired neural crest migration in a non-autonomous manner, as shown by *in situ* hybridization and graft experiments (Fig. 3e–g and Extended Data Fig. 5h–k; fibronectin controls in Extended Data Fig. 6c, f). In agreement with our hypothesis, cell densities and mesoderm stiffness were reduced in DshDEP$^+$-injected embryos (Fig. 3h–k).

To confirm that the inhibition of neural crest migration after blocking PCP is a consequence of a mechanical change in the tissue, we rescued mesodermal stiffness in the softer PCP-depleted embryos by applying sustained extrinsic compression with iAFM[12,18,19] (Fig. 4a). This was sufficient to completely rescue neural crest migration (Fig. 4b–d), and to promote premature neural crest migration (Extended Data Fig. 10). These results indicate that the impaired neural crest migration observed in PCP-depleted embryos was mainly due to the decreased mesodermal stiffness.

While previous *in vitro* studies have proposed that mechanical cues may promote EMT[10] and CCM[11], we show here that convergent extension of the mesoderm leads to local stiffening, which in turn works as a long-range signal, triggering EMT and CCM of the neural crest *in vivo* (Fig. 4e). It is well known that tissue mechanics are a key determinant in many biological processes, such as axon growth[12], central nervous system development[25] and maintenance of tissue integrity via cell–cell adhesion during collective cell movement[15,16,27,28]. The most common regulators of tissue stiffness include ECM accumulation[21,22], cortical contractility[13,16,17] and cell densities[12,25,26]. Here we identified cellular rearrangements driven by PCP-dependent convergent extension as a mechanism that increases cell densities to increase stiffness in a developing organism. Similar changes in tissue stiffness are likely to occur in other systems undergoing PCP-dependent convergent extension.

An exciting new area of research is related to the *in vitro* generation of organ-analogous structures called organoids[4,29,30]. This research has focused mainly on the molecular manipulation of homogenous cell populations and mechanical inputs are just starting to be considered in the field[29,30]. As our findings reveal that proper morphogenesis requires mechanical interactions between different tissues, we anticipate that the consideration of mechanical signals in the organoid field will increase the success of *ex vivo*-engineered tissues. Moreover, as CCM is a common mode of migration during development, regeneration, wound healing and cancer progression[1,2,15,16,24,28], it is tempting to speculate that mechanical cues from the surrounding tissues could also play an important role during CCM in these systems.

Online Content Methods, along with any additional Extended Data display items and Source Data, are available in the online version of the paper; references unique to these sections appear only in the online paper.

Received 17 March 2017; accepted 11 January 2018.
Published online 14 February 2018.

1. Roca-Cusachs, P., Sunyer, R. & Trepat, X. Mechanical guidance of cell migration: lessons from chemotaxis. *Curr. Opin. Cell Biol.* **25,** 543–549 (2013).
2. Mayor, R. & Etienne-Manneville, S. The front and rear of collective cell migration. *Nat. Rev. Mol. Cell Biol.* **17,** 97–109 (2016).
3. Kerosuo, L. & Bronner-Fraser, M. What is bad in cancer is good in the embryo: importance of EMT in neural crest development. *Semin. Cell Dev. Biol.* **23,** 320–332 (2012).
4. Gilmour, D., Rembold, M. & Leptin, M. From morphogen to morphogenesis and back. *Nature* **541,** 311–320 (2017).
5. Nieto, M. A., Huang, R. Y., Jackson, R. A. & Thiery, J. P. EMT: 2016. *Cell* **166,** 21–45 (2016).
6. Betancur, P., Bronner-Fraser, M. & Sauka-Spengler, T. Assembling neural crest regulatory circuits into a gene regulatory network. *Annu. Rev. Cell Dev. Biol.* **26,** 581–603 (2010).
7. Nieuwkoop, P. D. & Faber, J. *Normal Table of* Xenopus laevis *(Daudin): a Systematical and Chronological Survey of the Development from the Fertilized Egg till the End of Metamorphosis* 2nd edn (North-Holland, 1967).
8. Theveneau, E. *et al.* Collective chemotaxis requires contact-dependent cell polarity. *Dev. Cell* **19,** 39–53 (2010).
9. Alfandari, D., Cousin, H., Gaultier, A., Hoffstrom, B. G. & DeSimone, D. W. Integrin $\alpha5\beta1$ supports the migration of *Xenopus* cranial neural crest on fibronectin. *Dev. Biol.* **260,** 449–464 (2003).
10. Wei, S. C. *et al.* Matrix stiffness drives epithelial–mesenchymal transition and tumour metastasis through a TWIST1–G3BP2 mechanotransduction pathway. *Nat. Cell Biol.* **17,** 678–688 (2015).
11. Sunyer, R. *et al.* Collective cell durotaxis emerges from long-range intercellular force transmission. *Science* **353,** 1157–1161 (2016).
12. Koser, D. E. *et al.* Mechanosensing is critical for axon growth in the developing brain. *Nat. Neurosci.* **19,** 1592–1598 (2016).
13. Zhou, J., Kim, H. Y. & Davidson, L. A. Actomyosin stiffens the vertebrate embryo during crucial stages of elongation and neural tube closure. *Development* **136,** 677–688 (2009).
14. Barriga, E. H., Maxwell, P. H., Reyes, A. E. & Mayor, R. The hypoxia factor Hif-1α controls neural crest chemotaxis and epithelial to mesenchymal transition. *J. Cell Biol.* **201,** 759–776 (2013).
15. Rauzi, M., Verant, P., Lecuit, T. & Lenne, P. F. Nature and anisotropy of cortical forces orienting *Drosophila* tissue morphogenesis. *Nat. Cell Biol.* **10,** 1401–1410 (2008).
16. Bjerke, M. A., Dzamba, B. J., Wang, C. & DeSimone, D. W. FAK is required for tension-dependent organization of collective cell movements in *Xenopus* mesendoderm. *Dev. Biol.* **394,** 340–356 (2014).
17. Wang, N. *et al.* Mechanical behavior in living cells consistent with the tensegrity model. *Proc. Natl Acad. Sci. USA* **98,** 7765–7770 (2001).
18. Storm, C., Pastore, J. J., MacKintosh, F. C., Lubensky, T. C. & Janmey, P. A. Nonlinear elasticity in biological gels. *Nature* **435,** 191–194 (2005).
19. Pogoda, K. *et al.* Compression stiffening of brain and its effect on mechanosensing by glioma cells. *New J. Phys.* **16,** 075002 (2014).
20. Charras, G. & Sahai, E. Physical influences of the extracellular environment on cell migration. *Nat. Rev. Mol. Cell Biol.* **15,** 813–824 (2014).
21. Moeendarbary, E. *et al.* The soft mechanical signature of glial scars in the central nervous system. *Nat. Commun.* **8,** 14787 (2017).
22. Chevalier, N. R. *et al.* How tissue mechanical properties affect enteric neural crest cell migration. *Sci. Rep.* **6,** 20927 (2016).
23. Seufert, D. W., Hanken, J. & Klymkowsky, M. W. Type II collagen distribution during cranial development in *Xenopus laevis*. *Anat. Embryol. (Berl.)* **189,** 81–89 (1994).
24. Shindo, A. & Wallingford, J. B. PCP and septins compartmentalize cortical actomyosin to direct collective cell movement. *Science* **343,** 649–652 (2014).
25. Koser, D. E., Moeendarbary, E., Hanne, J., Kuerten, S. & Franze, K. CNS cell distribution and axon orientation determine local spinal cord mechanical properties. *Biophys. J.* **108,** 2137–2147 (2015).
26. Shyer, A. E. *et al.* Emergent cellular self-organization and mechanosensation initiate follicle pattern in the avian skin. *Science* **357,** 811–815 (2017).
27. Dzamba, B. J., Jakab, K. R., Marsden, M., Schwartz, M. A. & DeSimone, D. W. Cadherin adhesion, tissue tension, and noncanonical Wnt signaling regulate fibronectin matrix organization. *Dev. Cell* **16,** 421–432 (2009).
28. Weber, G. F., Bjerke, M. A. & DeSimone, D. W. A mechanoresponsive cadherin–keratin complex directs polarized protrusive behavior and collective cell migration. *Dev. Cell* **22,** 104–115 (2012).
29. Wrighton, P. J. & Kiessling, L. L. Forces of change: mechanics underlying formation of functional 3D organ buds. *Cell Stem Cell* **16,** 453–454 (2015).
30. Poh, Y. C. *et al.* Generation of organized germ layers from a single mouse embryonic stem cell. *Nat. Commun.* **5,** 4000 (2014).

Supplementary Information is available in the online version of the paper.

Acknowledgements We thank A. J. Thompson for assistance with the AFM. This study was supported by grants to R.M. from the Medical Research Council (J000655), Biotechnology and Biological Sciences Research Council (M008517) and Wellcome Trust; to K.F. from the Medical Research Council (Career Development Award G1100312/1) and from the Eunice Kennedy Shriver National Institute of Child Health & Human Development of the National Institutes of Health (R21HD080585); to G.C. from the European Research Council (Consolidator grant MolCellTissMech, agreement 647186); and by postdoctoral fellowships to E.H.B. from EMBO (LTF-971) and Marie Skłodowska Curie (IF-2014_ST VivoMechCollMigra, agreement 658536). The content is solely the responsibility of the authors and does not necessarily represent the official views of the National Institutes of Health.

Author Contributions E.H.B. and R.M. conceived the project, E.H.B., K.F., G.C. and R.M. designed the experiments. All the experiments and analyses were performed by E.H.B. E.H.B. and R.M. wrote the manuscript. All the authors edited the manuscript.

Author Information Reprints and permissions information is available at www.nature.com/reprints. The authors declare no competing financial interests. Readers are welcome to comment on the online version of the paper. Publisher's note: Springer Nature remains neutral with regard to jurisdictional claims in published maps and institutional affiliations. Correspondence and requests for materials should be addressed to R.M. (r.mayor@ucl.ac.uk).

Reviewer Information *Nature* thanks L. A. Davidson, N. Wang and the other anonymous reviewer(s) for their contribution to the peer review of this work.

METHODS

***Xenopus* manipulation, *in situ* hybridization and *in vitro* transcription.** *Xenopus* embryos were obtained as previously described[14]. In brief, ovulation of mature females was induced by injecting serum gonadotrophin (Intervet) and chorionic gonadotrophin (Intervet). Released eggs were collected and fertilized *in vitro* by mixing with a sperm solution. Embryonic stages were determined as described[7]. For *in situ* hybridizations, an antisense digoxigenin-labelled RNA probe against *snail2*[31], a neural crest marker, was used and embryos at non-migratory, pre-migratory or migratory stages were fixed, hybridized and stained using established protocols[32]. Templates for riboprobes and mRNAs were generated as previously described[14,32]. In brief, for mRNA transcription an mMESSAGE mMACHINE SP6 Transcription Kit (Thermo-Fisher AM1340) was used. The riboprobe against *snail2* was transcribed with a Riboprobe *in vitro* Transcription System (Promega P1420). All animal experiments were approved by the Biological Service Unit at University College London and complied with UK Home Office guidelines (Animal Act 1986).

Morpholino and mRNA injections and reagents. Microinjections were performed using calibrated needles as described[33]. Fertilized eggs were de-jellied for 5 min with a solution containing 1 g cysteine (Sigma) and 1 ml of 5N NaOH in 50 ml ddH_2O. For cell labelling, 10 nl nuclear RFP (nRFP) and/or membrane GFP (mGFP) mRNAs were injected at the two-cell stage into one blastomere (250 pg per embryo per construct). Vinculin-Cter and talin-Nter were previously validated[34] and injected at the eight-cell stage in one dorsal blastomere (500 pg per embryo per construct). *itgb1*-MO (5′-GAATACTGGATAA- CGGGCCATCTTA-3′) was synthesized by GeneTools (GeneTools) and injected as previously described[35]. For targeted injections to the mesoderm, two dorso-vegetal blastomeres were injected (as shown in Fig. 2e and Extended Data Fig. 4c). Embryos were injected with 5 pg per blastomere of a morpholino against *myl9*[24] (*myl9*-MO 5′-TGGCTTTTGTCTTCTTGCTGGACAT-3′), synthesized by GeneTools (GeneTools); 1 ng per blastomere of $DshDEP^+$ (ref. 24); 1 ng per blastomere of CA-MYPT[36]; or 1 ng per blastomere of CA-MLC[37], both kindly provided by M. Tada.

For blebbistatin incubations, embryos were incubated as indicated in Extended Data Fig. 9, in a solution containing 100 μM blebbistatin (ab12042) dissolved in dimethyl sulfoxide (DMSO, Thermo-Fisher).

***Ex vivo* neural crest culture, chemotaxis assay on glass and graft experiments.** Neural crests were dissected at non-migratory or pre-migratory stages as previously described[14]. In brief, 20 min prior to dissection the chorion was removed with fine forceps, embryos were placed in a dish containing modelling clay, and a hair knife was used to remove the epidermis and explant the neural crest. After dissection, neural crests were maintained in Danilchik's medium (DFA; 53 mM NaCl, 5 mM Na_2CO_3, 4.5 mM KGluconate, 32 mM NaGluconate, 1 mM $MgSO_4(7H_2O)$, 1 mM $CaCl_2$, 0.1% BSA; adjusted to pH 8.3 with 1 M Bicine). To test the response of neural crests to Sdf-1 we used a chemotaxis assay[8,38] in which acrylic heparin beads (Sigma-Aldrich) were coated overnight with 1 μg/ml Sdf-1 (Sigma-Aldrich), washed with PBS and fixed to a fibronectin-coated glass-bottom dish (μ-Dish, 35 mm high, Ibidi) using silicon grease. Fluorescently labelled explants (mRFP or mGFP) were placed two diameters away from the bead and migration was recorded by time-lapse microscopy.

For graft experiments, wild-type or treated neural crests from donor and host embryos were removed as described above; a hair knife was used to locate the donor neural crest in the host embryo and a piece of glass coverslip was used to hold the grafted neural crest. The coverslip was removed after 1 h and the embryos were mounted for live imaging. Embryos were mounted on agarose dishes containing 1.2-mm lanes with 4% methyl cellulose (Sigma-Aldrich) and filled with DFA medium.

Polyacrylamide hydrogels: preparation and functionalization. Polyacrylamide (PAA) gels were prepared as follows. To allow adhesion to PAA, 76 mm × 24 mm glass slides were coated overnight at room temperature in a solution containing 14:1:1 ethanol:acetic acid:PlusONE Bind-Silene (GE Healthcare; vol:vol:vol). The slides were washed twice with 70% ethanol, air dried and stored at room temperature. For hydrophobic coating, 13-mm diameter × 0.1 mm glass coverslips were air cleaned and coated for 15 min at room temperature with PlusONE Repel-Silene ES (GE Healthcare), carefully recovered, air-dried and used immediately.

PAA mixes were prepared as follows. For soft gels, a mix containing 550 μl 7.6 mM HCl, 369.5 μl ddH_2O, 0.5 μl N,N,N′,N′-tetramethylethylenediamine (TEMED, Sigma), 16 μl bis-acrylamide (BioRad) and 60 μl acrylamide (BioRad) was prepared. For stiff gels, a mix containing 550 μl 7.6 mM HCl, 349.5 μl ddH_2O, 0.5 μl TEMED, 20 μl bis-acrylamide and 75 μl acrylamide was prepared. Polymerization was started by adding 5 μl of 10% ammonium persulfate (GE Healthcare) to each mix.

Soft or stiff gels were obtained by placing a 12-μl drop of PAA mix on an adhesive slide and covering with a hydrophobic coverslip. Polymerization was allowed to proceed for 25 min at room temperarture in a humidifier and the coverslip was carefully removed. Gels were washed three times for 10 min with 10 mM HEPES buffer.

Fibronectin was covalently linked to soft or stiff gels via Sulfo-SANPAH-mediated succinimide cross-linking. To activate gels, aliquots containing 1 mg of Sulfo-SANPAH (Thermo-Fisher 22589) in 20 μl anhydrous DMSO (Thermo-Fisher D12345) were rapidly diluted in 480 μl of 10 mM HEPES buffer. From the resulting solution, 25 μl was added to the gel surface and gels were irradiated with ultraviolet light for 5 min. The excess of Sulfo-SANPAH was removed by washing for 5 min with 10 mM HEPES buffer. A drop containing 10 mg/ml fibronectin was added to the surface of the activated gels, covered with Parafilm, and incubated for 2 h in a humidifier. The parafilm was removed and the functionalized gels were washed twice for 5 min in 10 mM HEPES buffer. Young's modulus (in Pa) for each gel was determined by AFM and functionalization was checked by immunostaining against fibronectin (Extended Data Fig. 2k–m).

Chemotaxis and dispersion assays on hydrogels with varying stiffness values. *Chemotaxis.* To test how substrate stiffness contributes to the response of neural crest cells towards Sdf-1, we developed a chemotaxis assay on PAA gels of varying stiffness. In brief, once coated with Sdf-1 as described for the glass chemotaxis assay, acrylic heparin beads (Sigma-Aldrich) were split into two halves and each half was gently indented in the surface of fibronectin-coated PAA hydrogels (no differences in gel stiffness were observed upon bead indentation, controlled with AFM). Labelled neural crest explants were placed two to three diameters in front of the beads and migration was registered by time-lapse microscopy.

Dispersion assay. As a read-out of EMT we used a cell dispersion assay on PAA hydrogels of varying stiffness. In brief, labelled neural crests were explanted into fibronectin-coated hydrogels and allowed to disperse. Dispersion was recorded by time-lapse microscopy.

Immunostaining and phalloidin staining. For phospho-myosin (ab2480, Abcam) and fibronectin (mAb 4H2 anti-FN, kindly provided by D. DeSimone) immunostaining in flat-mounted embryos, whole embryos were fixed using 2% TCA (trichloroacetic acid) in 0.3% PBS-T (PBS, 0.3% Triton X-100) for 20 min. Dorsal halves of fixed embryos were dissected using a 15°, 5-mm depth microsurgical knife (MSP 7516). Dissected halves were washed with PBS and blocked for 4 h with 10% normal goat serum (NGS). Antibodies were diluted at 1:100 (anti-myosin) and 1:500 (anti-fibronectin) in 10% NGS and incubated overnight at 4 °C, followed by three washes with 0.3% PBS-T (PBS, 0.3% Triton X-100). Alexa-fluor (Thermo-Fisher) secondary antibodies were diluted 1:350 in 10% NGS and incubated overnight at 4 °C and excess antibody was removed by washing three times with 0.3% PBS-T. Nuclei were stained with DAPI in a mixture with the secondary antibodies (1:1,000). Finally, embryos were washed overnight in methanol and flat-mounted for imaging in clearing mix (two volumes benzyl alcohol and one volume benzyl benzoate; Sigma-Aldrich). For E-cadherin and N-cadherin detection, explants were fixed with 4% formaldehyde in 0.2% PBS-T (PBS, 0.2% Triton X-100) for 12 min and blocked with 10% NGS for 2 h. The primary antibody (anti-E-cadherin 5D3 or anti-N-cadherin MNCD2, Developmental Studies Hybridoma Bank) was diluted at 1:100 in 10% NGS and incubated overnight at 4 °C. Explants were washed three times with 0.2% PBS-T and incubated overnight at 4 °C with secondary antibody, diluted at 1:350 in 10% NGS. DAPI was diluted at 1:1,000 and mixed with the secondary antibodies. To detect fibronectin on gels, functionalized gels were washed twice with PBS and incubated for 1 h at room temperature with anti-human fibronectin (Sigma S3648) diluted 1:500 in PBS. Gels were washed three times with PBS and incubated for 1 h at room temperature with 1:350 Alexa-fluor anti-Rabbit 488 and 1:1,000 DAPI. Gels were washed three times with PBS and maintained in 1% formaldehyde in PBS. Fluorescence intensity was analysed using the measurement tool from ImageJ.

Phalloidin (Thermo Fisher A12379) staining was carried out as follows: embryos were fixed in a mix containing 4% paraformaldehyde and 0.25% glutaraldehyde for 10 min, washed three times in 0.3% PBS-T for 10 min and incubated in a solution containing 5U phalloidin per ml PBS. Excess phallodin was washed with 0.3% PBS-T and embryos were dehydrated in isopropanol (10 min) and cleared and mounted in 2:1 benzyl benzoate:benzyl alcohol (Sigma).

Microscopy and time-lapse live-imaging. *Time-lapse imaging.* Images for chemotaxis and dispersion assays (on gels and glass) were acquired every 5 min at 18 °C using an upright microscope (DMR XA2, Leica) equipped with a motorized stage (Prior Scientific) and a camera (Orca-5G Hamamatsu). Filter wheels, camera, stage and shutters were controlled with SimplePCI software (Hamamatsu). A 20× objective (HCX APO L 20×/0.50 W U-V-I FWD = 3.50 mm, Leica) was used.

Confocal time-lapse imaging. Images were acquired every 16 s at 18 °C using an upright confocal integrated microscope system (SP8vis, Leica) with a 63× objective (HCX APO L 63×/0.90 W U-V-I CS2, FWD = 2.20 mm, Leica).

Live imaging. For graft experiments, time-lapse images were acquired every 10 min with an upright microscope (Eclipse 80i, Nikon) fitted with a motorized stage

(Prior Scientific) and a camera (ORCA-05G, Hamamatsu Photonics). Images were acquired at 18 °C with a 4× objective (CFI Plan Fluor 4×/0.13, WFD = 17.1 mm). Camera, stage, shutter and filter wheels were controlled with SimplePCI software (Hamamatsu).

In situ hybridization imaging. All images were captured at room temperature in agarose dishes containing PBS, using a dissecting microscope (MZ FL III, Leica) equipped with a camera (DFL420, Leica) and imaging software (IM50, Leica). Magnification was 3.2×.

Immunofluorescence imaging. All images were acquired at room temperature. Images in Fig. 3a, b, j, k and Extended Data Figs 2b, f; 4d, g; 6; 9e, f were acquired in an inverted confocal microscope (FluoView FV1000, Olympus) equipped with a digital camera (DP73, Olympus) and a 20× objective (UPLSAPO 20×/0.75 FWD = 0.6 mm, Olympus). Camera, filter wheels, and shutters were controlled by FluoView Software (Olympus). Confocal images in Extended Data Figs 2k and 3 were acquired using an upright confocal integrated microscope system (SP8vis, Leica) with a 63× objective (HC PL APO 63×/1.40 Oil CS2, FWD = 0.14 mm, Leica).

***In vivo* atomic force microscopy measurements.** All AFM measurements were carried out as previously described[12,21,25,40]. In brief, a JPK Nanowizard Cellhesion 200 (JPK Instruments AG), fitted with a x–y-motorized stage and mounted on an inverted optical microscope (Axio ObserverA1, Zeiss) was used. Customized cantilevers were used. For mesoderm AFM measurements, tipless silicon cantilevers (Arrow-TL1, NanoWorld) were mounted on the AFM device and spring constants were calculated using the thermal noise method[39]. Cantilevers with spring constants between 0.01 and 0.03 N/m were selected. Monodisperse polystyrene beads (diameter: 37.28 ± 0.34 μm; microParticles) were glued to the selected cantilevers[12,21,25]. Embryos were mounted on a clay modelling dish and the epidermis was carefully dissected using a hair knife. Force–distance curves were acquired every 15 μm in the region immediately lateral to the neural crest as shown in Fig. 1g and Extended Data Fig. 2g. A region of interest was defined using a custom-written script that controls the x–y-motorized stage (maximum indentation force: 7 nN, approach speed: 5 μm/s, data rate: 1,000 Hz). Measurements on intact embryos were carried out in the same territory, but embryos were not dissected. In these experiments, monodisperse polystyrene beads (diameter: 89.3 ± 1.1 μm; microParticles GmbH) were glued to tipless silicon cantilevers with spring constants of ~0.1 N/m (Shocon-TL; AppNano), and force–distance curves were acquired with a maximum indentation force of 50 nN, approach speed: 5 μm/s, data rate: 1,000 Hz, one measurement per embryo. For extrinsic compression experiments, stress was applied in the same region where measurements were taken (Fig. 2m) with 89.3 ± 1.1 μm beads as cantilever probes. A sustained force of 80 nN (control embryos) and 50 nN (DshDEP$^+$-injected embryos) was applied to compress the tissue. Force was applied until embryos reached pre-migratory (control and DshDEP$^+$) or migratory stages (DshDEP$^+$). Uncompressed time-matched embryos and the contralateral side of the compressed embryos were used as controls. An image was acquired for each measurement using an adapted AxioZoom V.16 system (Zeiss) connected to an Andor Zyla 4.2 CMOS camera. After compression, embryos were rapidly fixed for *in situ* hybridization. Displacement maps were generated using the ImageJ iterative PIV basic plugin.

Data analysis and image treatment. *AFM data.* Force–distance curves were analysed as previously described, using a customized Matlab routine based on the Hertz model for a spherical indenter[12,21,25]

$$F = \frac{4}{3} K \sqrt{r} \delta^{3/2} = \frac{4}{3} \frac{E}{1-\nu^2} \sqrt{r} \delta^{3/2}$$

with applied force F, Young's modulus E, Poisson's ratio ν, indenter radius r, indentation depth δ, and apparent elastic modulus $K = E/(1-\nu^2)$, which is referred to as 'apparent elasticity' in the text. Force–distance curves from the measurements taken in the region of interest were analysed for defined indentation depths of 3 μm, which has been shown to measure the mechanical properties of developing tissues[12,21,25,40]. The mean maximum indentation depth is included in each figure. Measurements for each experiment were pooled and statistically analysed. Representative examples of force curves with highlighted indentation depths (δ) are provided (Extended Data Fig. 2i, j). Mean indentation depth (δ) for each AFM experiment is included below the corresponding charts.

***In vivo* analysis of neural crest migration.** For *in situ* hybridized embryos, the length of the treated neural crest was normalized against the length of the contralateral control side of the embryo. For grafted embryos, the length of the neural crest was normalized against the total dorsoventral length of the embryo at the position of the neural crest. Lengths were obtained using the measurement tool from ImageJ and further analysed as described in Statistical analysis.

***Ex vivo* analysis of neural crest migration.** Manual tracking and chemotaxis tool plugins from ImageJ were used to calculate speeds of migration. For dispersion assays, an ImageJ-based custom-made Delaunay-triangulation plugin[13] was used to calculate the distance between neighbour cells (available upon request). Data were further analysed as described in Statistical analysis.

Cell density measurements. Confocal images of transverse sections stained for DAPI were projected in ImageJ. A region of interest (ROI) was selected in the mesoderm under the neural crest in embryos at non-migratory stages; the number of nuclei within this region was quantified and nucleus density was calculated as the number of nuclei within the ROI divided by the area of the ROI. The same ROI size was used to calculate density at stage 17 and pre-migratory stages. Cell density was expressed in nuclei per μm^2.

Image treatment. *z*-stacks, maximum projections and time-lapse movies were created using ImageJ software. Adjustment of display map levels, re-sizing, addition of scale bars and pseudocolour were applied with ImageJ and/or Adobe Photoshop. In Fig. 2c, g, h, k, o, and 3a (pre-migratory *in situ* hybridization panel) and Fig. 4b, the background was pseudocoloured in Photoshop.

Cryosectioning. Fixed embryos were washed twice for 5 min with phosphate buffer (0.2 M $NaH_2PO_4 \cdot H_2O$ and 0.2 M K_2HPO_4, pH 7.4), and incubated for 2 h at room temperature with a solution containing 15% sucrose (wt/vol; Sigma-Aldrich) in phosphate buffer and for 1 h at 42 °C in a gelatin solution containing 8% gelatin (Sigma-Aldrich) and 15% sucrose in phosphate buffer (wt/vol). Embryos were oriented in gelatin solution and gelatin blocks containing the embryos were snap frozen at −80 °C with pre-chilled isopentane. Samples were sectioned in 20-μm slices using a cryostat (CM-3050S, Leica) and collected in SuperFrozen Slides (VWR International). The slides were dried for at least 6 h and the gelatin was removed by washing twice with PBS for 15 min. MOWIOL (EMD Millipore) was used as mounting medium.

Statistical analysis. Sample size was determined by following published studies and no statistical method was used. The experiments were not randomized. Owing to the nature of the experiments, the authors were not blinded to allocation during experiments and results analysis, and only viable embryos and cell clusters were included for analysis. Additionally, mis-injected embryos were excluded from *in situ* hybridization analysis (correct injection was monitored by co-injection of linear tracing molecules mRFP or fluorescein dextran (FDX)). After selecting surviving and properly injected embryos and/or cells, our parameters for different experiments were measured at random.

Each experiment was repeated at least three times. Normality in the spread of data for each experiment was tested using the Kolmogorov–Smirnov, d'Agostino–Pearson or Shapiro–Wilk test in Prism7 (GraphPad). Significances for datasets displaying normal distributions were calculated in Prism7 with an unpaired Student's *t*-test (two-tailed, unequal variances) or one-way analysis of variance (ANOVA) for multiple comparisons. Individual comparisons were calculated only when ANOVA showed $P < 0.05$. Significances for non-normal distributed data were calculated in Prism7 using the Mann–Whitney *U*-test.

Data and code availability. Original data that support our findings and custom codes for analysis are available from the corresponding author upon reasonable request. Source Data for *P* values are provided in the online version of the paper.

31. Mayor, R., Morgan, R. & Sargent, M. G. Induction of the prospective neural crest of *Xenopus*. *Development* **121,** 767–777 (1995).
32. Harland, R. M. *In situ* hybridization: an improved whole-mount method for *Xenopus* embryos. *Methods Cell Biol.* **36,** 685–695 (1991).
33. Mancilla, A. & Mayor, R. Neural crest formation in *Xenopus laevis*: mechanisms of *Xslug* induction. *Dev. Biol.* **177,** 580–589 (1996).
34. Iioka, H., Iemura, S., Natsume, T. & Kinoshita, N. Wnt signalling regulates paxillin ubiquitination essential for mesodermal cell motility. *Nat. Cell Biol.* **9,** 813–821 (2007).
35. Morita, H. *et al.* Cell movements of the deep layer of non-neural ectoderm underlie complete neural tube closure in *Xenopus*. *Development* **139,** 1417–1426 (2012).
36. Weiser, D. C., Row, R. H. & Kimelman, D. Rho-regulated myosin phosphatase establishes the level of protrusive activity required for cell movements during zebrafish gastrulation. *Development* **136,** 2375–2384 (2009).
37. Di Ciano-Oliveira, C. *et al.* Is myosin light-chain phosphorylation a regulatory signal for the osmotic activation of the Na^+–K^+–$2Cl^-$ cotransporter? *Am. J Physiol. Cell. Physiol.* **289,** C68 –C81 (2005).
38. Theveneau, E. & Mayor, R. Beads on the run: beads as alternative tools for chemotaxis assays. *Methods Mol. Biol.* **769,** 449–460 (2011).
39. Hutter, J. & Bechhoefer, J. Calibration of atomic-force microscope tips. *Rev. Sci. Instrum.* **64,** 1868–1873 (1993).
40. Iwashita, M., Kataoka, N., Toida, K. & Kosodo, Y. Systematic profiling of spatiotemporal tissue and cellular stiffness in the developing brain. *Development* **141,** 3793–3798 (2014).
41. Benko, R. & Brodland, G. W. Measurement of in vivo stress resultants in neurulation-stage amphibian embryos. *Ann. Biomed. Eng.* **35,** 672–681 (2007).
42. Goto, T., Davidson, L., Asashima, M. & Keller, R. Planar cell polarity genes regulate polarized extracellular matrix deposition during frog gastrulation. *Curr. Biol.* **15,** 787–793 (2005).

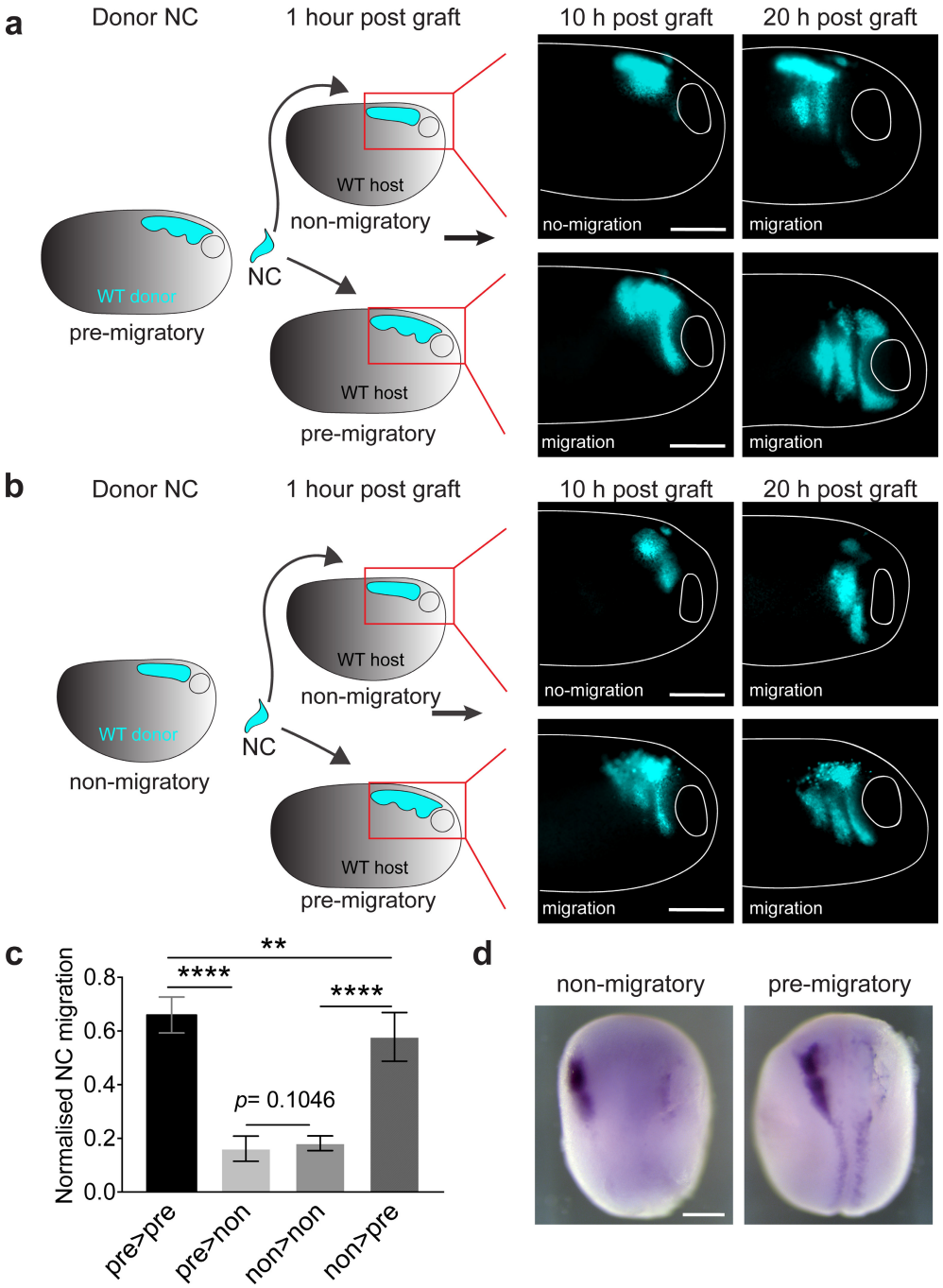

Extended Data Figure 1 | Neural crest migration is controlled by environmental factors. a–d, Heterochronic graft controls. In all grafts, we completely removed the host neural crest before implanting the graft, and all grafted cells migrated 20 h post graft, as expected for embryos reaching the migratory stage[7] (stage 23). **a**, Labelled pre-migratory neural crest grafted into unlabelled non- and pre-migratory hosts. Ten hours post graft, representative examples show that pre-migratory neural crest grafted into non-migratory hosts does not migrate and that pre-migratory neural crest grafted into pre-migratory hosts does migrate. **b**, Labelled non-migratory neural crest grafted into unlabelled non- and pre-migratory hosts. Ten hours post graft, representative examples show that non-migratory neural crests grafted into non-migratory hosts do not migrate and that pre-migratory neural crests grafted into pre-migratory hosts do migrate. Twenty hours post-graft panels in **a** and **b** show that neural crests migrated in all conditions after 20 h. **c**, Normalized neural crest migration. Histograms show mean, error bars represent s.d.; $n = 80$ measurements from 20 embryos (one-way ANOVA, $P < 0.0001$; two-tailed t-test, $^{**}P = 0.0026$, $^{****}P < 0.0001$, CI = 95%). **d**, Dorsal views of embryos hybridized with a probe against *snail2* after dissection of the host neural crest, showing that endogenous neural crest was completely removed before grafting. **a**, **b** and **d** show representative examples of three independent experiments; scale bar, 250 μm.

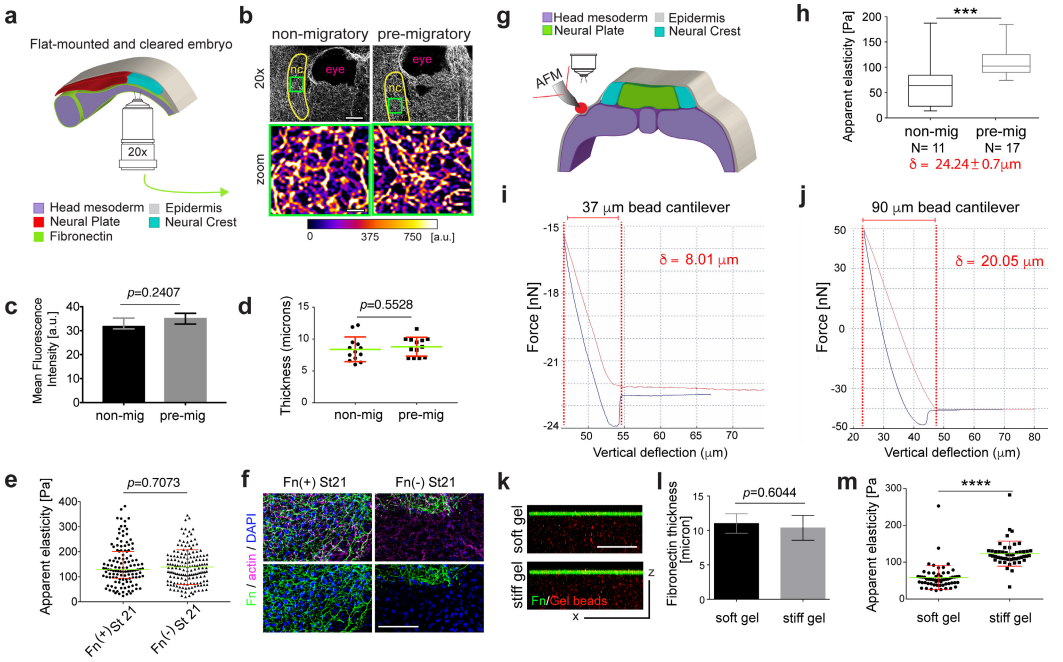

Extended Data Figure 2 | Fibronectin expression under the neural crest *in vivo* and contribution to tissue stiffness, stiffness measurements across epidermis, and *ex vivo* system characterization. a–d, Analysis of fibronectin expression under the neural crest. **a**, Schematic showing the imaging method used to access fibronectin under the neural crest. **b**, Immunostaining for fibronectin in embryos at non- and pre-migratory stages. 20× panels, yellow outline highlights the anatomical position of the neural crest; green box highlights the region shown in the zoom panels. Zoom panels show heat maps of fibronectin signal (representative of five independent samples). **c**, Fluorescence signal intensity. Histograms show mean, error bars represent s.d. (two-tailed *t*-test, CI = 95%). **d**, Fibronectin signal thickness in the mesoderm at pre- and non-migratory stages. Green lines show median and red whiskers represent interquartile range; $n = 10$ embryos (**c**), $n = 26$ sections from three independent experiments (**d**) (two-tailed *t*-test, CI = 95%). Scale bars: 50 μm (20× panels), 20 μm (zoom panels). **e**, **f**, Apparent elasticity was measured before and after mechanical removal of the ECM by gently scraping the surface of the tissue with a hair loop. **e**, Apparent elasticity was measured directly on the mesoderm in the presence ($Fn^{(+)}$) or absence ($Fn^{(-)}$) of fibronectin (Fn, green) in embryos at stage 21 (pre-migratory). Graphs plot spread of data; green lines show median; red whiskers represent interquartile range. Two-tailed Mann–Whitney *U*-test, *P* as indicated, CI = 95%; n = number of AFM indentations: $n = 124$ ($Fn^{(+)}$), $n = 157$ ($Fn^{(-)}$). Mean indentation depth = 8 μm. **f**, Representative immunostaining against fibronectin (Fn), conditions as indicated, $n = 7$ embryos. Scale bar, 100 μm. **g**, **h**, AFM controls. **g**, Schematic of iAFM measurement. To check that the dissection of the epidermis did not modify the mesodermal elasticity, we measured the elastic modulus through the epidermis, and no differences were found (compare with Fig. 1h). **h**, Apparent elasticity. Box plots show the median, box edges represent the 25th and 75th percentiles, and whiskers show the spread of data (excluding outliers). Two-tailed Mann–Whitney *U*-test, $***P = 0.0006$, CI = 95%; n = number of embryos, δ = mean indentation depth. **i**, **j**, Representative examples of force curves obtained from measurements performed using cantilevers coated with either 37-μm beads (**i**, $n = 2386$) or 90-μm beads (**j**, $n = 28$). Red lines represent cantilever extension and dark blue lines represent retraction. Indentation depth (δ) for each curve is provided. **k**–**m**, *Ex vivo* system characterization. **k**, Cross-sectional confocal image of stiff or soft PAA hydrogels, confirming that gels (red) of varying stiffness are evenly functionalized with fibronectin (green). **l**, Fibronectin thickness does not change between soft and stiff gels. Histograms represent mean and bars show s.d.; $n = 8$ gels; two-tailed *t*-test, CI = 95%. Results in **k** and **l** are representative of gels from three independent experiments. **m**, AFM measurements. Spread of data, green lines show median, red whiskers represent interquartile range; two-tailed Mann–Whitney *U*-test, $****P < 0.0001$, CI = 95%; $n = 60$ (stiff), $n = 50$ (soft) from 10 gels. Scale bars, 50 μm (**k**).

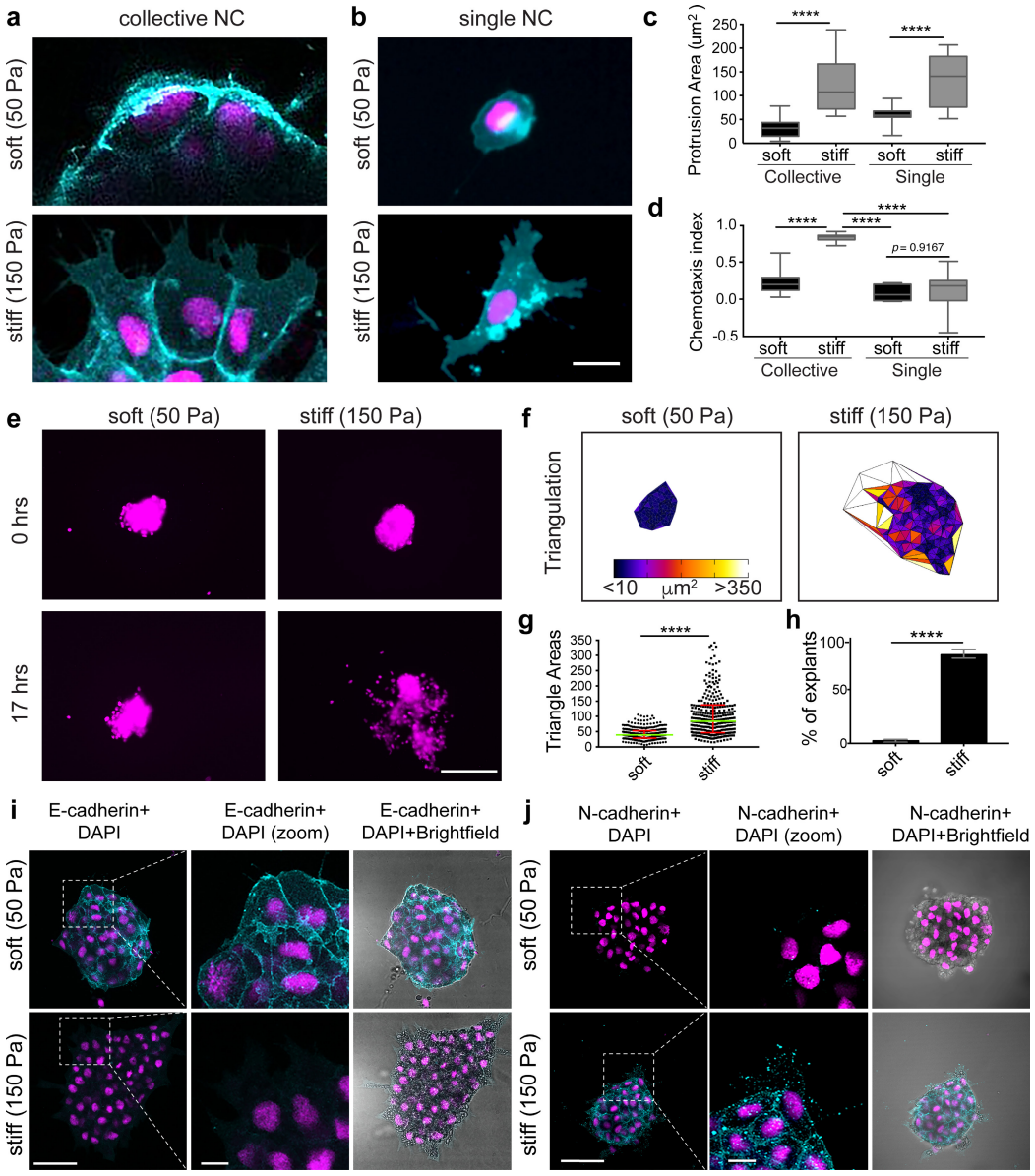

Extended Data Figure 3 | Neural crest motility, dispersion and EMT are controlled by substrate mechanics. a–d, Protrusion and chemotaxis analysis of collective and single neural crest cells plated on soft and stiff substrates. **a**, Confocal projections of labelled neural crest collectives plated on soft or stiff gels. **b**, Confocal projections of labelled single neural crest cells plated on soft or stiff gels. Protrusion area (**c**) and chemotaxis quantifications (**d**) for collective and single neural crest cells plated on soft or stiff gels, box plots show median, box edges represent 25th and 75th percentiles and whiskers show the spread of data (excluding outliers). $n = 63$ cells (protrusion area), $n = 79$ cells (chemotaxis); one-way ANOVA, $P < 0.0001$; two-tailed t-test, $^{****}P < 0.0001$, CI = 95%. **e–h**, Neural crest dispersion analysis on gels of varying stiffness. **e**, Neural crest cells labelled with nRFP and plated on stiff or soft gels are shown at 0 h and 17 h after plating. **f–h**, Quantification of cell dispersion. **f**, Colour-coded Delaunay triangulation shown at 17 h after plating to facilitate visualization of the distances between neighbour cells. **g**, Quantification of Delaunay triangulation. Green lines show median, red whiskers represent the interquartile range; two-tailed Mann–Whitney U-test, $^{****}P < 0.0001$, CI = 95%; $n = 730$ triangles from 31 explants. **h**, Percentage of dispersing explants. Histograms show mean and error bars represent s.e.m.; two-tailed t-test, $^{****}P < 0.0001$, CI = 95%; $n = 31$ explants. **g** and **h** show data from four independent experiments (soft) and three independent experiments (stiff). **i**, **j**, Immunostaining for E-cadherin (**i**) and N-cadherin (**j**) on neural crests plated on substrates of varying stiffness. **a**, **b**, **e**, **i** and **j** show representative examples from three independent experiments. Scale bars: 20 μm (**a**, **b**), 250 μm (**e**), 50 μm (**i**, **j**, main), 10 μm (**i**, **j**, zoom).

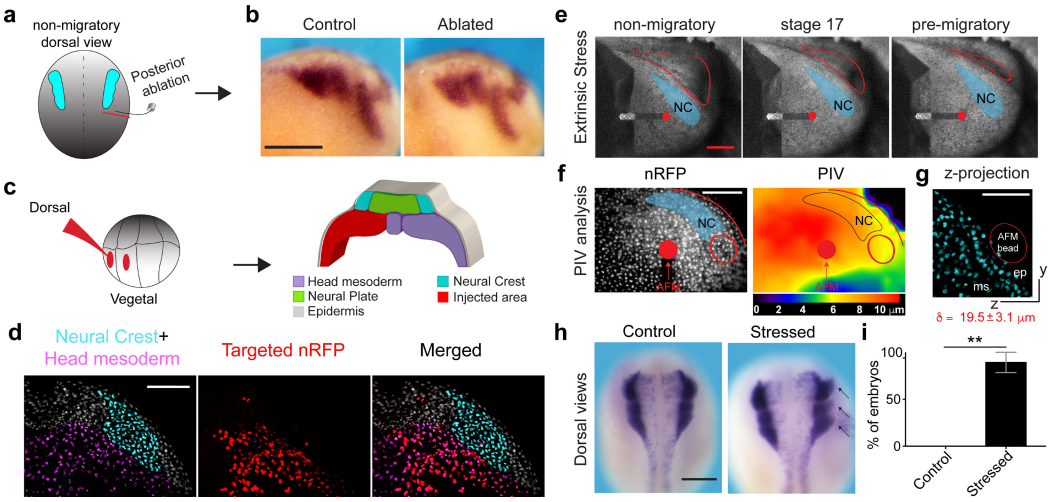

Extended Data Figure 4 | Posterior ablations, mesoderm targeted injections and extrinsic compression characterization. a, **b**, Ablation controls. Mechanical tension in *Xenopus* is higher in the anterior region of the embryo than in posterior territories[12,41]. Consistent with this observation, no effect on neural crest migration or tissue stiffness was observed when the ablation was done in posterior regions. **a**, Schematic showing embryos ablated at non-migratory stages, and neural crest migration at stage 23 (migratory)[7]. **b**, Lateral views of control and posterior-ablated embryos hybridized with a probe against *snail2*. Scale bar, 250 µm. **c**, **d**, Targeted injections into the head mesoderm. **c**, Cartoon shows that injecting two dorso-vegetal blastomeres targets the head mesoderm. **d**, Confocal images of targeted injections showing nuclear RFP expression in the mesoderm. Scale bar, 100 µm. **e**–**g**, Compression controls. **e**, Images of embryos being compressed from non-migratory to pre-migratory stages with a 90-µm bead attached to an AFM cantilever (bead, red circumference). Neural plate border highlighted with red lines and neural crest position shown in light blue; stages as labelled. **f**, Magnitude maps from a particle image velocity (PIV) analysis indicates the *x*–*y* extent of the deformation induced by AFM indentation. **g**, Maximum projection of a cross-section showing the *z*-deformation generated by the AFM compression. Epidermis (ep) and mesoderm (ms) are being deformed, mean maximum indentation depth (δ) is provided (nuclei are visible in the bead region owing to a maximum projection effect). **h**, **i**, Result of extrinsic stress experiments. **h**, Dorsal view (anterior to top) of embryos hybridized with a probe against *snail2*; black arrows point to migrating neural crest. **i**, Percentage of embryos displaying neural crest migration. Histograms show mean, error bars represent s.e.m.; $n = 13$ embryos; two-tailed *t*-test, $^{**}P = 0.001$, CI = 95%. All experiments repeated three times. Scale bars: 200 µm (**e**, **f**), 100 µm (**g**), 200 µm (**h**).

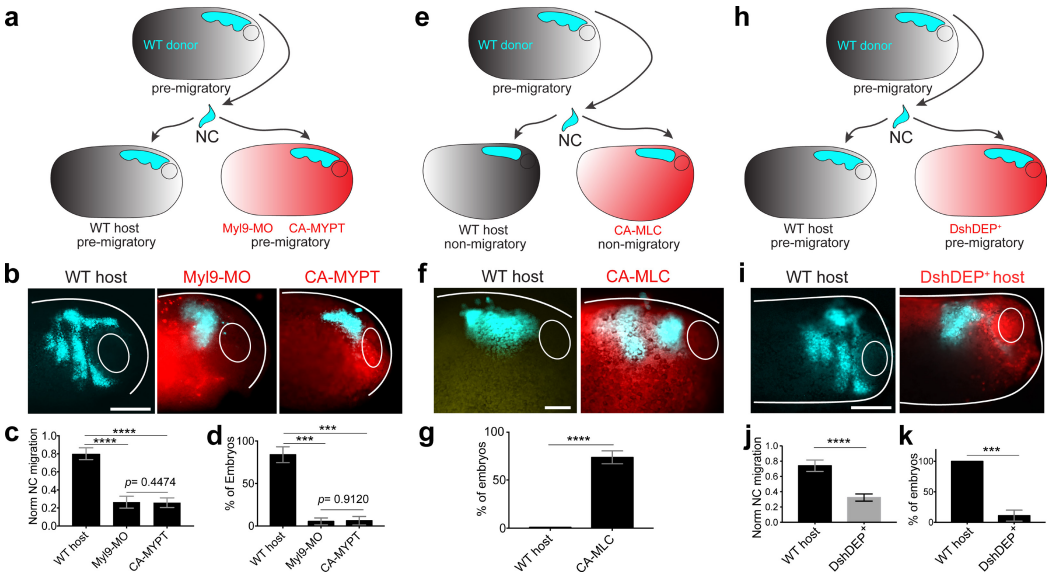

Extended Data Figure 5 | Mesodermal stiffening promotes neural crest CCM in a non-autonomous manner *in vivo*. **a**–**d**, Non-autonomous effect of mesodermal myosin manipulations on neural crest migration *in vivo*. **a**, Wild-type labelled pre-migratory neural crest (cyan) grafted into pre-migratory wild-type, *myl9*-MO or CA-MYPT-injected hosts (mesoderm in red). **b**, Representative embryos showing normal neural crest migration in wild-type hosts and inhibited neural crest migration in *myl9*-MO or CA-MYPT hosts. Scale bar, 200 μm. **c**, **d**, Normalized neural crest migration (**c**, $n = 22$ embryos) and percentage of embryos displaying neural crest migration (**d**, $n = 38$ embryos) (**c**, **d**; one-way ANOVA, $P < 0.0001$; two-tailed *t*-test, $^{***}P < 0.0006$, $^{****}P < 0.0001$, CI = 95%). Histograms in **c**, **d** and **g** show mean, error bars represent s.d. (**c**) or s.e.m. (**d**, **g**). **e**–**g**, Effect of premature mesodermal stiffening on neural crest migration *in vivo*. **e**, Wild-type labelled pre-migratory neural crest grafted into non-migratory wild-type or CA-MLC hosts. **f**, Representative embryos showing premature neural crest migration in CA-MLC hosts, whereas no migration is observed in control embryos at this stage. Scale bar, 100 μm. **g**, Percentage of embryos displaying neural crest migration. Two-tailed *t*-test, $^{****}P < 0.0001$, CI = 95%, $n = 20$ embryos. **h**–**k**, Non-autonomous effect of DshDEP^{+} on neural crest migration. **h**, Wild-type labelled pre-migratory neural crest (cyan) was grafted into pre-migratory wild-type or DshDEP^{+} hosts. **i**, Representative examples showing neural crest migration in wild-type hosts and inhibited neural crest migration in DshDEP^{+}-injected hosts (mesoderm in red). Scale bar, 150 μm. Normalized neural crest migration (**j**) and percentage of embryos displaying neural crest migration (**k**) (**j**, **k**; two-tailed *t*-test, $^{***}P < 0.0002$, $^{****}P < 0.0001$, CI = 95%, $n = 14$ embryos). Histograms in **j** and **k** show mean, error bars represent s.d. (**j**) and s.e.m. (**k**). **b**, **f** and **i** are representative examples of three independent experiments.

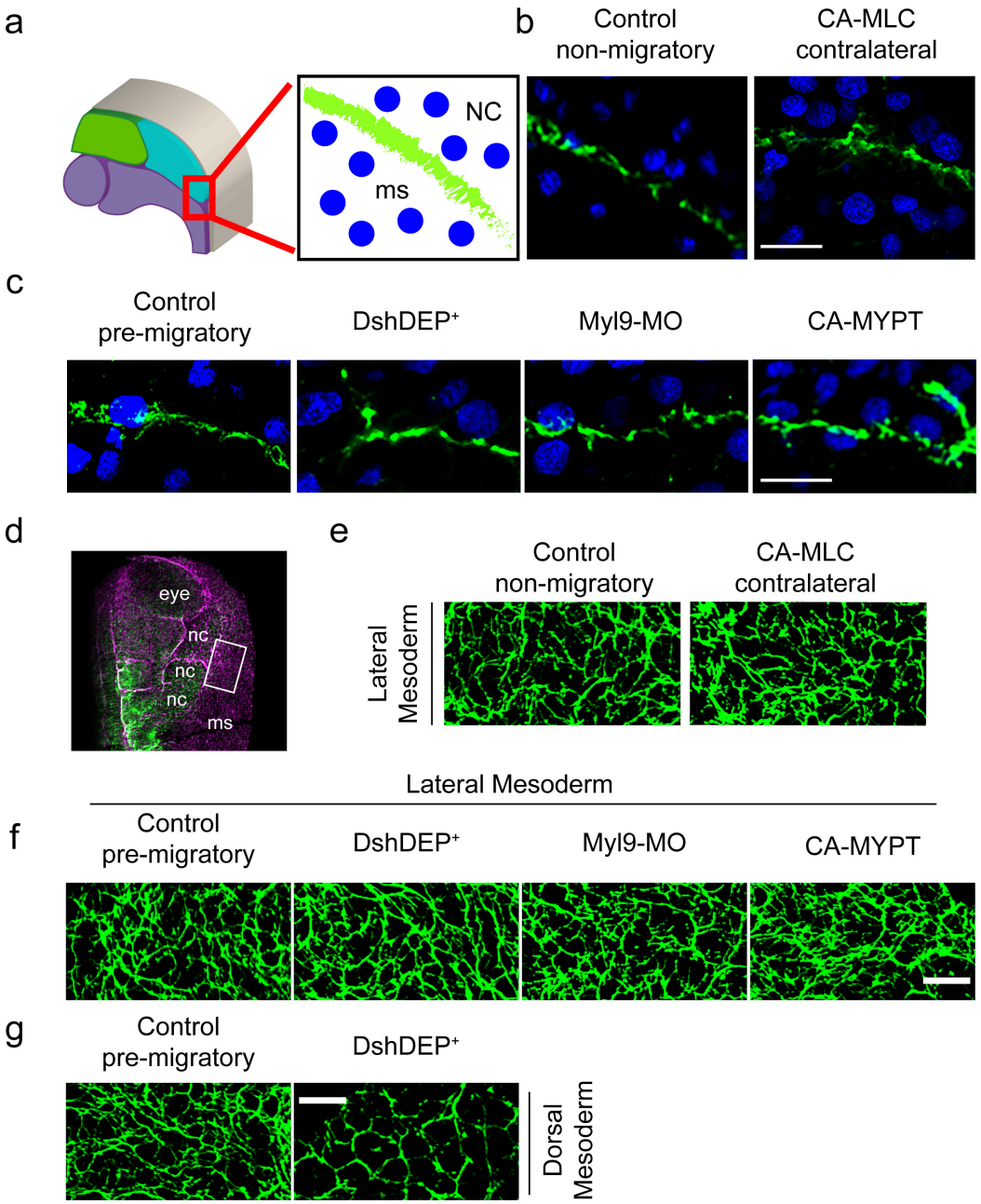

Extended Data Figure 6 | Head mesoderm manipulations did not affect fibronectin deposition and organization under the neural crest. As it has been previously shown that inhibition of myosin and PCP can affect fibronectin deposition and organization in the dorsal mesoderm[27,28,42]; we analysed the effect of these treatments on the lateral mesoderm underlying the premigratory neural crest. Our results show no effect of inhibition of myosin or PCP on fibronectin deposition or organization in the lateral mesoderm, indicating that the effect of our treatments on neural crest migration are not due to an indirect effect on fibronectin, but rather a consequence of affecting mesoderm stiffness. **a**–**c**, Transverse sections showing fibronectin expression with different treatments used to manipulate the apparent elasticity of head mesoderm. **a**, Schematic showing the area presented in **b** and **c**. **b**, **c**, Immunostaining against fibronectin (green) and DAPI stain (blue) showing the fibronectin signal underneath the neural crest, treatments as labelled in each panel. Scale bar, 30 μm. **d**–**g**, Effect of mesoderm manipulation on fibronectin assembly. **d**, Dorsal view of a flat-mounted embryo. White square indicates the area shown in **e** and **f**. **e**, Immunostaining against fibronectin (green) in non-migratory embryos (stage 13), showing fibronectin assembly underneath the neural crest, treatments as indicated. **f**, Immunostaining against fibronectin (green) in pre-migratory embryos (stage 20) showing fibronectin assembly underneath the neural crest, treatments as indicated. Control to show that inhibition of PCP signalling (DshDEP^{+}) affects fibronectin assembly in dorsal mesoderm[42] (**g**) but not lateral mesoderm (**f**). Scale bars, 30 μm. **b**, **c** and **e**–**g** are representative examples of three independent experiments.

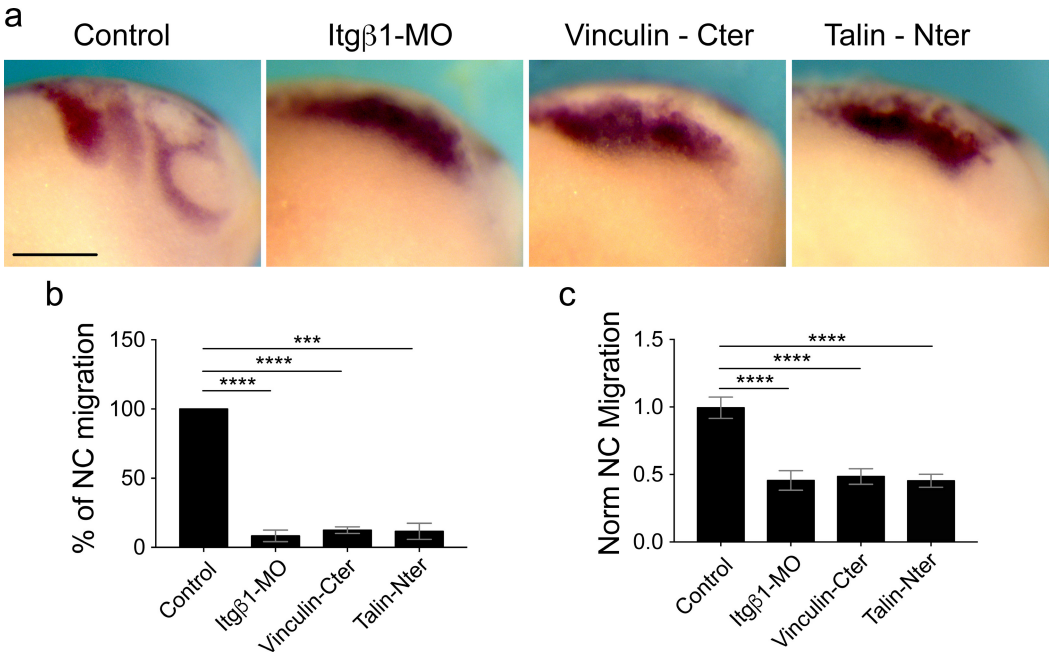

Extended Data Figure 7 | Neural crest senses mesoderm stiffening by using an integrin–vinculin–talin-mediated mechanoresponsive mechanism. a–c, Analysis of neural crest migration after integrin β1, vinculin or talin knockdown. **a**, Lateral views of embryos hybridized with a probe against *snail2*. Control embryos migrate normally from dorsal to ventral. However, neural crest migration is drastically inhibited in embryos treated with itgβ1-MO or the dominant-negative mutants vinculin-Cter and talin-Nter. Embryos in **a** are representative examples of three independent experiments. **b**, **c**, Quantification of neural crest migration showing percentage of embryos (**b**) and normalized neural crest migrated distances (**c**). Histograms in **b** and **c** show mean, error bars represent s.e.m. (**b**) and s.d. (**c**); one-way ANOVA, $P < 0.0001$; two-tailed *t*-test, $^{***}P < 0.0002$ $^{****}P < 0.0001$, CI = 95%; $n = 39$ embryos. Scale bar, 200 μm.

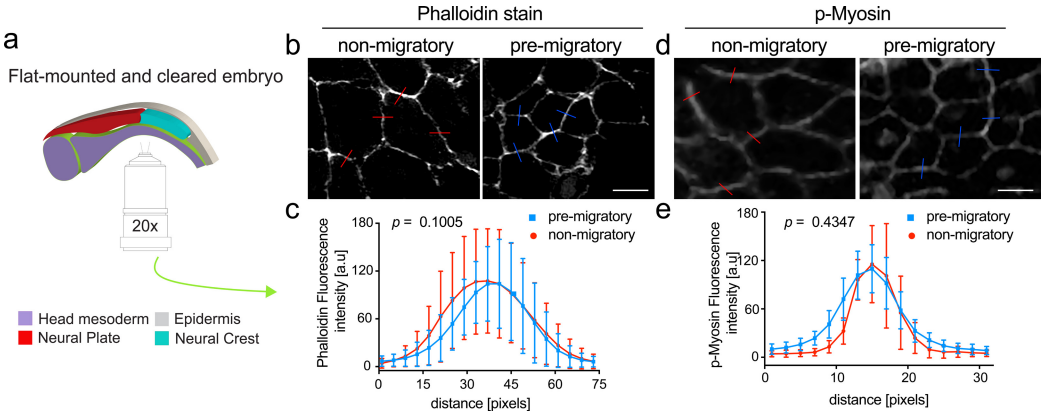

Extended Data Figure 8 | Actomyosin expression in the head mesoderm does not change from non- to pre-migratory stages. a–e, Analysis of actin and phospho-myosin expression under the neural crest. As actomyosin contractility has been proposed to contribute to paraxial mesoderm stiffness in *Xenopus*[13], we assessed actomyosin activity in the head mesoderm, the substrate of the neural crest. Note that the expression levels of either actin or phospho-myosin remained unchanged at pre-migratory stages compared to non-migratory stages. **a**, Schematic showing the imaging method used to access the head mesoderm under the neural crest. **b**, Phalloidin stain was used to label actin on embryos at non- and pre-migratory stages. **d**, Immunostaining against phospho-myosin on embryos at non- and pre-migratory stages. **c**, **e**, Quantification of fluorescence intensity across the membrane in **b** and **d**, respectively, represented by a continuous line. Points show mean and error bars represent s.d.; *n*, number of measurements per data (time) point; $n = 16$ (**c**), $n = 15$ (**e**); from three independent experiments; non-significant differences were observed, *P* value is indicated in each chart (two-tailed *t*-test, CI = 95%). Scale bars, 20 μm.

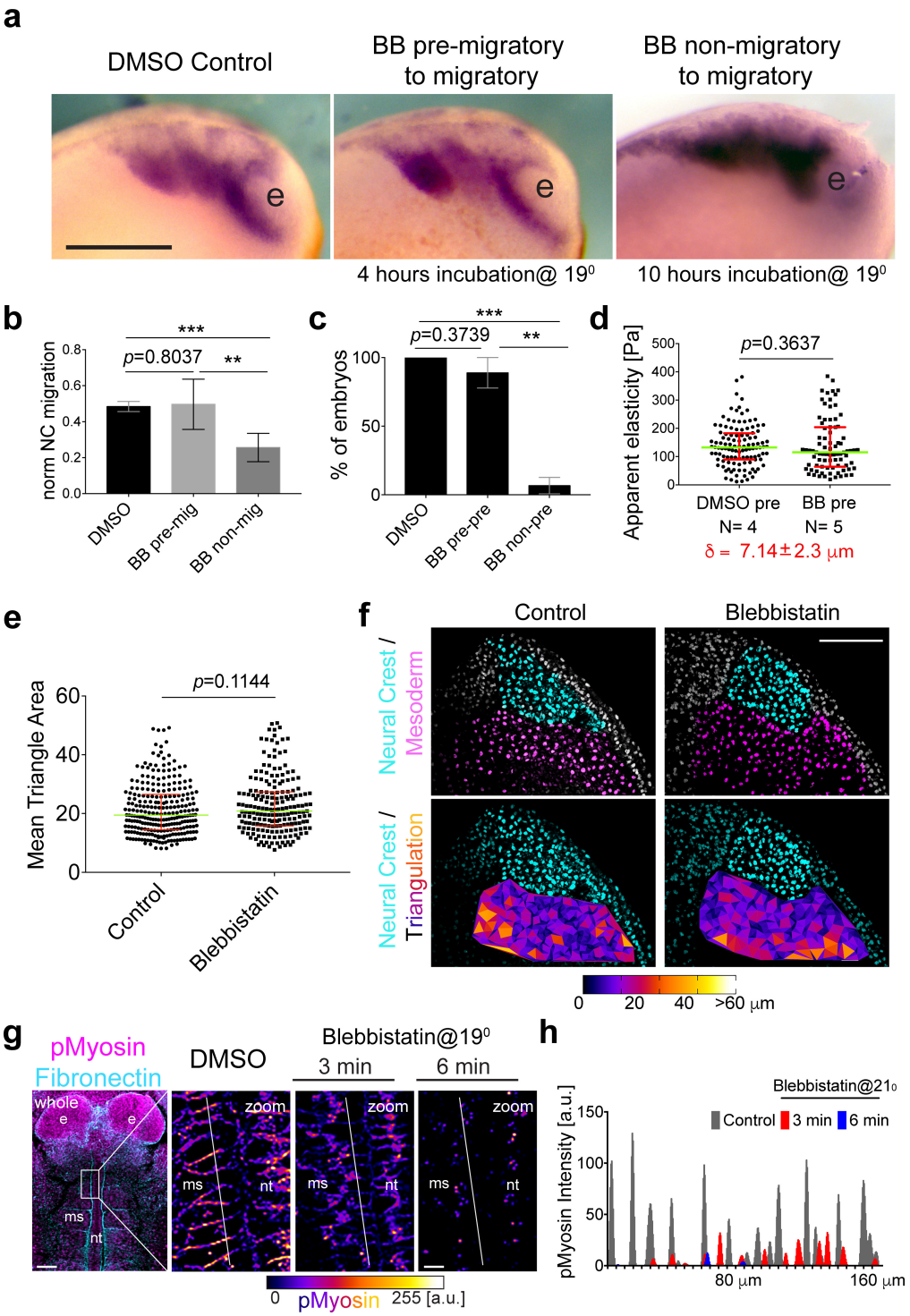

Extended Data Figure 9 | Myosin contractility is not required to maintain mesodermal stiffness. a–f, Blebbistatin incubation experiments. To functionally test the effect of actomyosin contractility on mesoderm stiffness, we applied blebbistatin to pre-migratory embryos. Note that blebbistatin treatment at this stage did not affect mesoderm stiffness, cell density or neural crest migration, in spite of a marked reduction in myosin phosphorylation. **a**, Lateral views of embryos hybridized with a probe against *snail2*, showing no differences in neural crest migration after 4 h of incubation with DMSO or blebbistatin (BB). Embryos were incubated as indicated. Scale bar, 150 μm. Normalized neural crest migration (**b**) and percentage of embryos (**c**). In **b** and **c**, histograms show mean and error bars represent s.d. (**b**) and s.e.m. (**c**); one-way ANOVA, $P < 0.0001$; two-tailed *t*-test $^{**}P < 0.008$, $^{***}P < 0.002$, CI = 95%, $n = 19$ embryos. **d**, iAFM measurement direct on mesoderm. Spread of data plotted for each condition; green lines show median, red whiskers represent the interquartile range (two-tailed Mann–Whitney *U*-test, *P* value as indicated, CI = 95%; *n* = number of AFM indentations, $n = 116$ (DMSO), $n = 204$ (BB_pre). **e**, **f**, As blebbistatin treatment could potentially affect cell–cell adhesion, thus promoting cell dispersion, we measured its effect on cell dispersion by calculating the distance between neighbouring mesoderm cells. **e**, Chart comparing the mean area of the triangle formed by each mesoderm cell with its neighbours, calculated by Delaunay triangulation (Mann–Whitney *U*-test, *P* value is shown). *n* = number of embryos, δ = mean maximum indentation depth. **f**, Images showing representative neural crest and mesoderm cells (treated as indicated) and triangles from which the areas in **e** were calculated. Scale bar, 200 μm. **g**, Immunostaining for phospho-myosin; dorsal view of a flat-mounted embryo and colour-coded intensity of zoom images at the indicated time points are shown (scale in arbitrary units, a.u.). Scale bars, 100 μm (whole), 15 μm (zoom). **h**, Fluorescence intensity in a.u. across the white line in the zoom panels in **g**. All experiments repeated at least three times. Images in

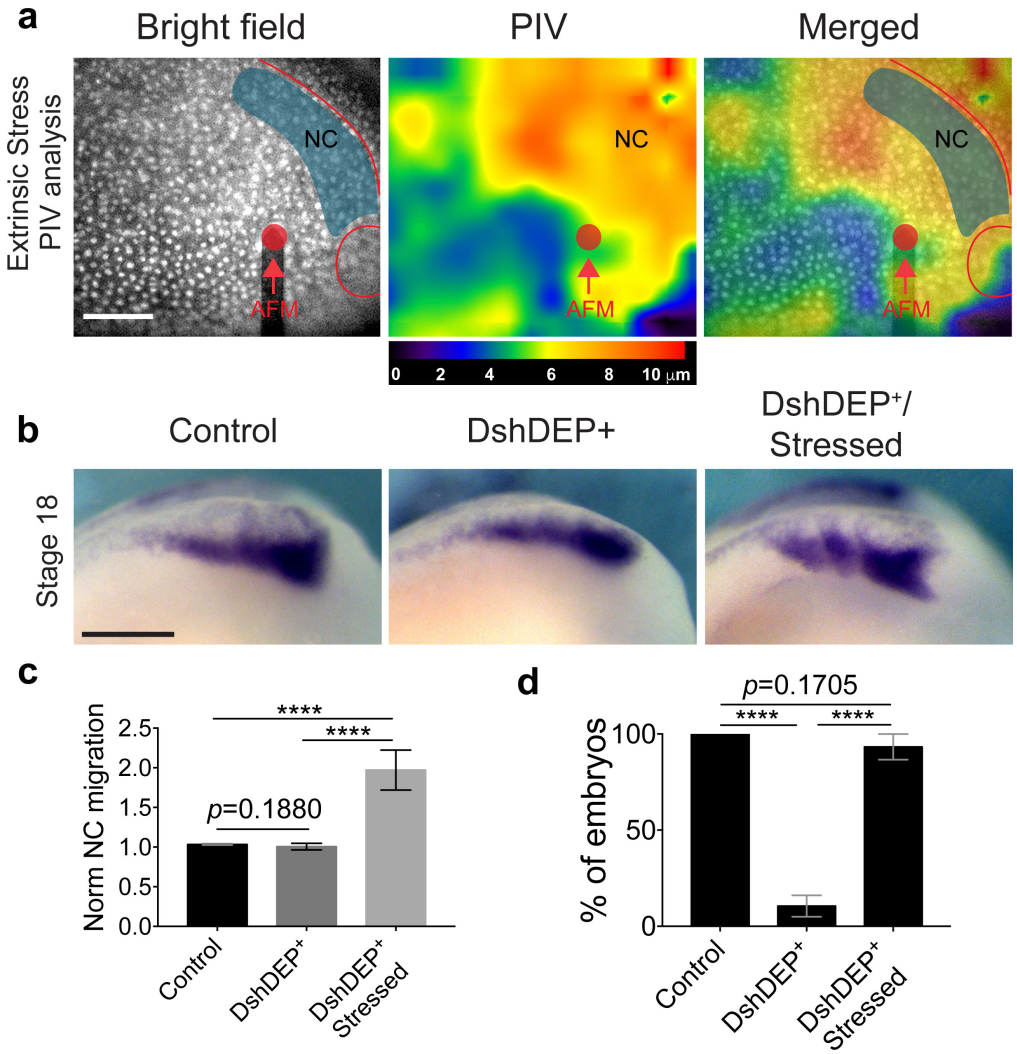

Extended Data Figure 10 | Extrinsic compression modifies the environment of PCP-depleted embryos and triggers premature neural crest CCM *in vivo*. **a**, Magnitude maps from a particle image velocity (PIV) analysis showing the *x*–*y* extent of the stress field generated by the extrinsic compression experiment. Neural plate border is indicated by red lines, neural crest is shown in light blue. Scale bar, 200 μm. **b**, **c**, Extrinsic stress-induced premature neural crest migration. **b**, Lateral views of embryos hybridized with a probe against *snail2*. Note that premature neural crest migration is observed in the DshDEP^{+}/stressed panel. Normalized neural crest migration (**c**) and percentage of embryos displaying each phenotype (**d**). Histograms show mean, error bars show s.d.(**c**) and s.e.m. (**d**); one-way ANOVA, $P < 0.0001$; two-tailed *t*-test, $^{****}P < 0.0001$, CI = 95%, $n = 18$ embryos. **a** and **b** show representative images of three independent experiments. Scale bar, 150 μm.

nature research

Corresponding author(s): Prof Roberto Mayor

☐ Initial submission ☐ Revised version ☒ Final submission

Life Sciences Reporting Summary

Nature Research wishes to improve the reproducibility of the work that we publish. This form is intended for publication with all accepted life science papers and provides structure for consistency and transparency in reporting. Every life science submission will use this form; some list items might not apply to an individual manuscript, but all fields must be completed for clarity.

For further information on the points included in this form, see Reporting Life Sciences Research. For further information on Nature Research policies, including our data availability policy, see Authors & Referees and the Editorial Policy Checklist.

Experimental design

1. Sample size

Describe how sample size was determined.

Specified in the methods section, Statistical analysis.
Sample size chosen by following the literature in the field.

2. Data exclusions

Describe any data exclusions.

Stated in the methods section, Statistical analysis. We excluded from our analyses unviable cells and embryos. Miss injected embryos were also excluded from in situ hybridisation.

3. Replication

Describe whether the experimental findings were reliably reproduced.

Once the protocols were established, all attempts of replication were successfully reproduced.

4. Randomization

Describe how samples/organisms/participants were allocated into experimental groups.

After selecting surviving and/or properly injected embryos or cells, the parameters for different experiments were measured at random. Stated in the methods section, Statistical Analysis.

5. Blinding

Describe whether the investigators were blinded to group allocation during data collection and/or analysis.

Authors were not blinded because embryos and cells were selected prior analysis. Criteria for selection was survival and correct delivery of the injected treatments. Stated in the Statistical Analysis section of the methods.

Note: all studies involving animals and/or human research participants must disclose whether blinding and randomization were used.

6. Statistical parameters

For all figures and tables that use statistical methods, confirm that the following items are present in relevant figure legends (or in the Methods section if additional space is needed).

n/a	Confirmed
☐	☒ The exact sample size (*n*) for each experimental group/condition, given as a discrete number and unit of measurement (animals, litters, cultures, etc.)
☐	☒ A description of how samples were collected, noting whether measurements were taken from distinct samples or whether the same sample was measured repeatedly
☐	☒ A statement indicating how many times each experiment was replicated
☐	☒ The statistical test(s) used and whether they are one- or two-sided (note: only common tests should be described solely by name; more complex techniques should be described in the Methods section)
☒	☐ A description of any assumptions or corrections, such as an adjustment for multiple comparisons
☐	☒ The test results (e.g. *P* values) given as exact values whenever possible and with confidence intervals noted
☐	☒ A clear description of statistics including central tendency (e.g. median, mean) and variation (e.g. standard deviation, interquartile range)
☐	☒ Clearly defined error bars

See the web collection on statistics for biologists for further resources and guidance.

Software

Policy information about availability of computer code

7. Software

Describe the software used to analyze the data in this study.	Prism7 and excel were used to statistically analyse data. PCI, Fluoview, Sp8, were used to acquire data. ImageJ was used to quantify imaging data and to generate the custom code used for triangulations (availability statement provided).

For manuscripts utilizing custom algorithms or software that are central to the paper but not yet described in the published literature, software must be made available to editors and reviewers upon request. We strongly encourage code deposition in a community repository (e.g. GitHub). *Nature Methods* guidance for providing algorithms and software for publication provides further information on this topic.

Materials and reagents

Policy information about availability of materials

8. Materials availability

Indicate whether there are restrictions on availability of unique materials or if these materials are only available for distribution by a for-profit company.	Original data that support our findings and analysis custom codes are available upon reasonable request to the corresponding author. Source Data for p values are provided in the online version of the paper. Also included in the Data Availability section in Methods.

9. Antibodies

Describe the antibodies used and how they were validated for use in the system under study (i.e. assay and species).	Anti-Myosin light chain (phospho S20) antibody (ab2480), validated in Shindo et al 2014, Sicence. [1:100]. Anti-E-Cadherin (5D3), DSHB. Validated in Barriga et al 2013, JCB. [5ug/ml]. Anti-N-cadherin (MNCD2) DSHB. Validate in Theveneau et al 2013, NCB. [5ug/ml]. Anti-Fibronectin (mAb 4H2) DSHB. Validated in Alfandari et al 2003, Dev Biol. [5ug/ml]. Anti-Fibronectin (F3648) SIGMA. Used for IF of human Fn in Sunyer et al 2016 [1/200]. Also stated in the methods section Immunostaining.

10. Eukaryotic cell lines

a. State the source of each eukaryotic cell line used.	No Eukaryotic cell lines were used in this study.
b. Describe the method of cell line authentication used.	No Eukaryotic cell lines were used in this study.
c. Report whether the cell lines were tested for mycoplasma contamination.	No Eukaryotic cell lines were used in this study.
d. If any of the cell lines used are listed in the database of commonly misidentified cell lines maintained by ICLAC, provide a scientific rationale for their use.	No Eukaryotic cell lines were used in this study.

Animals and human research participants

Policy information about studies involving animals; when reporting animal research, follow the ARRIVE guidelines

11. Description of research animals

Provide details on animals and/or animal-derived materials used in the study.	Adults female Xenopus laevis were use to obtain oocytes that were fertilised with sperm obtained from adult males. Embryos used in this study were at Xenopus neurula stages 13, 17, and 23 (defined as non-, pre-migratory, and migratory stages, respectively).

Policy information about studies involving human research participants

12. Description of human research participants

Describe the covariate-relevant population characteristics of the human research participants.	This study did not involve the use of human research participants.